Mon. Not. R. Astron. Soc. **360,** 1355–1372 (2005) doi:10.1111/j.1365-2966.2005.09139.x

Regularized orbit models unveiling the stellar structure and dark matter halo of the Coma elliptical NGC 4807

J. Thomas,[1,2]★ R. P. Saglia,[2] R. Bender,[1,2] D. Thomas,[2] K. Gebhardt,[3] J. Magorrian,[4] E. M. Corsini[5] and G. Wegner[6]

[1] *Universitätssternwarte München, Scheinerstraße 1, D-81679 München, Germany*
[2] *Max-Planck-Institut für Extraterrestrische Physik, Giessenbachstraße, D-85748 Garching, Germany*
[3] *Department of Astronomy, University of Texas at Austin, C1400, Austin, TX78712, USA*
[4] *Theoretical Physics, Department of Physics, University of Oxford, 1 Keble Road, Oxford OX1 3NP*
[5] *Dipartimento di Astronomia, Università di Padova, vicolo dell'Osservatorio 2, I-35122 Padova, Italy*
[6] *Department of Physics and Astronomy, 6127 Wilder Laboratory, Dartmouth College, Hanover, NH 03755-3528, USA*

Accepted 2005 April 14. Received 2005 March 22; in original form 2004 November 2

ABSTRACT

This is the second in a series of papers dedicated to unveiling the mass structure and orbital content of a sample of flattened early-type galaxies in the Coma cluster. The ability of our orbit libraries to reconstruct internal stellar motions and the mass composition of a typical elliptical in the sample is investigated by means of Monte Carlo simulations of isotropic rotator models. The simulations allow a determination of the optimal amount of regularization needed in the orbit superpositions. It is shown that under realistic observational conditions and with the appropriate regularization, internal velocity moments can be reconstructed to an accuracy of ≈15 per cent; the same accuracy can be achieved for the circular velocity and dark matter fraction. In contrast, the flattening of the halo remains unconstrained. Regularized orbit superpositions are applied to a first galaxy in our sample, NGC 4807, for which stellar kinematical observations extend to $3\,r_{\rm eff}$. The galaxy seems dark-matter dominated outside $r > 2\,r_{\rm eff}$. Logarithmic dark matter potentials are consistent with the data, as well as NFW profiles, mimicking logarithmic potentials over the observationally sampled radial range. In both cases, the derived stellar mass-to-light ratio Υ agrees well with independently obtained mass-to-light ratios from stellar population analysis. The achieved accuracy is $\Delta\Upsilon \approx 0.5$. Kinematically, NGC 4807 is characterized by mild radial anisotropy outside $r > 0.5\,r_{\rm eff}$, becoming isotropic towards the centre. Our orbit models hint at either a distinct stellar component or weak triaxiality in the outer parts of the galaxy.

Key words: stellar dynamics – galaxies: elliptical and lenticular, cD – galaxies: kinematics and dynamics – galaxies: structure.

1 INTRODUCTION

Interpreting the stellar kinematical data of ellipticals in terms of galaxy structural parameters requires knowing the gravitational potential as well as the distribution of stellar orbits, which – due to projection effects – is not directly given by observations. In equilibrium stellar systems, the phase-space distribution function (DF) describing the orbital state depends on phase-space coordinates only through the integrals of motion, admitted by the actual potential (Jeans' theorem; e.g. Binney & Tremaine 1987).

In cases where integrals of motion can be expressed (or, approximated) in terms of elementary functions, the DF can be parametrized explicitly. Several round as well as a couple of flattened ellipticals have been modelled based on this approach (e.g. Dehnen & Gerhard 1994; Carollo et al. 1995; Qian et al. 1995; Dejonghe et al. 1996; Gerhard et al. 1998; Emsellem, Dejonghe & Bacon 1999; Matthias & Gerhard 1999; Statler, Dejonghe & Smecker-Hane 1999; Kronawitter et al. 2000; Saglia et al. 2000; Gerhard et al. 2001). On the other hand, the orbit superposition modelling technique of Schwarzschild (1979) provides fully general dynamical models for *any* axisymmetric or triaxial potential and has been successfully applied to a growing number of early-type galaxies (e.g. Rix et al. 1997; Cretton & van den Bosch 1998; Cretton, Rix & de Zeeuw 2000; Gebhardt et al. 2000; Cappellari et al. 2002; Verolme et al. 2002; Gebhardt et al. 2003; Romanowsky et al. 2003; Copin, Cretton & Emsellem 2004; Valluri, Merritt & Emsellem 2004; Krajnović et al. 2005).

Even if the number of dynamical models is steadily increasing, the only comprehensive investigation of elliptical galaxy DFs

★E-mail: jthomas@mpe.mpg.de

addressing the question of dark matter in these systems is still the basis-function based spherical modelling of 21 round galaxies by Kronawitter et al. (2000) and Gerhard et al. (2001). To extend the results found there and in the handful of studies of individual objects quoted above, we started a project aimed at probing a sample of *flattened* early-type galaxies in the Coma cluster, collecting major (Mehlert et al. 2000) and minor axis (Wegner et al. 2002) kinematical data. The goal is to investigate the dynamical structure and dark matter content of these galaxies.

Most present-day orbit superpositions, conceptually based on Schwarzschild's original implementation, do not automatically provide the entire phase-space DF, but only orbital occupation numbers or weights, respectively, characterizing the total amount of light carried by each orbit. In principle, changing the orbit sampling strategy allows one to infer the DF from any orbit superposition (Häfner et al. 2000), but this approach has not yet been followed fully. To take advantage of both, the full generality of orbit superpositions and the availability of DFs, we extended the orbit superposition code of Richstone & Tremaine (1988) and Gebhardt et al. (2000) to reconstruct phase-space DFs in the axisymmetric case (Thomas et al. 2004).

Recovering stellar DFs from photometric and kinematic observations – in particular the application of non-parametric methods like orbit superpositions – invokes regularization in order to pick up smooth phase-space distributions (e.g. Richstone & Tremaine 1988; Merritt 1993). Different regularization schemes have been applied in the context of orbit libraries, among them variants of minimizing occupation number gradients in orbit space (Zhao 1996) and maximum entropy (Richstone & Tremaine 1988). The proper amount of regularization has thereby commonly been adjusted to the data (e.g. Rix et al. 1997; Verolme et al. 2002; Richstone et al., in preparation).

One aim of this paper is to readdress the question of how much regularization is needed to recover galaxy internal structural properties from observations with spatial sampling and noise typical for our sample of Coma galaxies. To this end we study observationally motivated reference models under realistic observational conditions and optimize regularization with respect to the reconstruction of intrinsic input-model properties (see, e.g. Gerhard et al. 1998; Cretton et al. 1999). By simulating and recovering reference galaxies we also determine to what degree the internal mass structure and orbital content are constrained by observational data in our sample. Furthermore χ^2-statistics are measured to assign confidence intervals to real galaxy orbit superpositions.

To demonstrate the prospects of regularized orbit superpositions for our project we also present an application to one galaxy. We have chosen the faint giant E2 elliptical NGC 4807 ($M_B = -20.76$ for $H_0 = 69\,\mathrm{km\,s^{-1}\,Mpc^{-1}}$ from Hyperleda) for the following reasons. (1) The galaxy has a prominent boxy photometric feature in the outer parts constraining its inclination. (2) Stellar kinematic data reach out to $3r_{\mathrm{eff}}$ along the major axis, probing its dark halo outside the main body of the galaxy. (3) NGC 4807 lacks significant minor-axis rotation and isophotal twist and thus is an ideal target for axisymmetric modelling. (4) The galaxy is only mildly flattened and the dynamical models can be compared with earlier studies of similar galaxies done mostly in the spherical approximation.

The paper is organized as follows. Section 2 summarizes the observations of NGC 4807, Section 3 outlines the orbit superposition technique. In Section 4 Monte Carlo simulations performed to derive the optimal regularization are described and the achieved accuracy of galaxy reconstructions follows in Section 5. Orbit models for NGC 4807 are presented in Sections 6–8. The paper closes with a combined summary and discussion of the results in Section 9.

2 NGC 4807: MODEL INPUT

In the following we assume a distance $d = 100$ Mpc to NGC 4807 (corresponding to $H_0 = 69\,\mathrm{km\,s^{-1}\,Mpc^{-1}}$) and take $r_{\mathrm{eff}} = 6.7$ arcsec as its effective radius (Mehlert et al. 2000).

2.1 Photometric data

The photometric data are combined from two different sources. For the outer parts of NGC 4807, Kron–Cousins R_C band CCD photometry is drawn from Mehlert et al. (2000), consisting of profiles for the surface brightness μ_R, ellipticity ϵ and isophotal shape parameters a_4 and a_6 out to $\approx 5.5\,r_{\mathrm{eff}}$ (see Bender & Möllenhoff 1987 for a definition of a_n). A seeing of 2 arcsec during the observations causes the profiles to be unresolved in their central parts (at $d = 100$ Mpc, one arcsec corresponds to 0.485 kpc). To increase the central resolution, the ground-based data are supplemented by corresponding profiles for μ_V, ϵ, a_4 and a_6 extracted from archival *HST V*-band data (Principal Investigator: John Lucey; Proposal ID: 5997).

The two surface brightness profiles μ_R and μ_V are joined by shifting the *HST V*-band according to the average $\langle \mu_R - \mu_V \rangle$ taken over the region $0.75\,r_{\mathrm{eff}} \leqslant R \leqslant 3\,r_{\mathrm{eff}}$, where both data sets overlap and seeing effects are negligible. The shift $\langle \mu_R - \mu_V \rangle$ is well defined with a rms of only 0.015 mag.

For the orbit models, ground-based photometry is used outside $R \geqslant 3\,r_{\mathrm{eff}}$ and *HST* data inside $R < 3\,r_{\mathrm{eff}}$. Fig. 1 shows the combined μ_R, ϵ, a_4 and a_6 profiles applied for the modelling.

2.2 Deprojection

In the implementation of Schwarzschild's modelling technique used here, orbit models are not directly fitted to observed photometry. Instead, the deprojected luminosity density is used as a boundary condition for any orbit superposition (see Section 3.4).

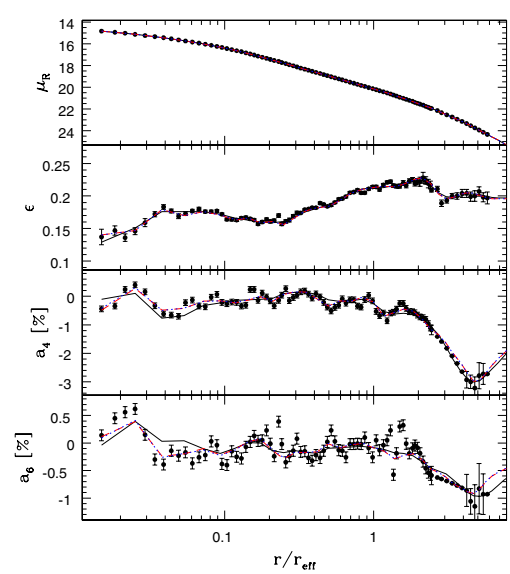

Figure 1. Photometric data for NGC 4807 (dots with error bars, from top to bottom: surface brightness μ_R, ellipticity ϵ, isophotal shape parameters a_4 and a_6) and three deprojections: edge-on deprojection (solid); $i = 50°$ deprojection (dashed); discy $i = 50°$ deprojection (dotted).

Deprojection of axisymmetric galaxies is unique only for edge-on systems (inclination $i = 90^\circ$; Rybicki 1987). For any inclination $i < 90^\circ$ disc-like konus densities can be added to the luminosity profile without affecting its projected appearance for any $i' < i$ (Gerhard & Binney 1996). From $i = 90^\circ$ to $i = 0^\circ$ the variety of different luminosity models projecting to the same galaxy image generally increases.

Deprojections for NGC 4807 are obtained with the program of Magorrian (1999). The code allows one to explore the full range of luminosity densities consistent with the photometric data by forcing the deprojection towards different internal shapes. For example, at any given inclination i the goodness of fit of the deprojection can be penalized towards any degree of internal boxiness and disciness, respectively. The deprojections are fitted without seeing correction, since our joint photometry includes ground-based data only outside $R \geqslant 3\,r_{\rm eff}$, where seeing effects are negligible. Outside the last measured photometric data point ($R \geqslant 5.5\,r_{\rm eff}$), the photometry is extrapolated by a de Vaucouleurs profile fitted to the inner parts of the galaxy. The isophotes outside $R > 5.5\,R_{\rm eff}$ are assumed to be perfect ellipses with a constant flattening corresponding to the outermost measured ellipticity of the galaxy.

From the average flattening $\langle q \rangle = 0.8$ of NGC 4807 we expect an inclination angle $i > 38^\circ$. Lower viewing angles would require density distributions intrinsically flatter than E7, which are not observed. In Fig. 1 three representative deprojections are overplotted on the photometric data: the (unique) $i = 90^\circ$ deprojection; a deprojection at $i = 50^\circ$ without any shape penalty; a discy $i = 50^\circ$ deprojection. All three luminosity models are equally consistent with the data. The differences between the models are illustrated in Fig. 2, which displays the isophotal shape parameters and the corresponding isophotes of the deprojections as they appear viewed from edge-on. At this viewing angle internal density distortions show up the strongest.

As Fig. 2 reveals, both deprojections at $i = 50^\circ$ are heavily boxy around $R \approx 2\,r_{\rm eff}$ ($a_4 \approx -10$ per cent for the deprojection without shape preference and $a_4 \approx -8$ per cent for the discy deprojection). These distortions are a reflection of the drop in a_4 at $R > 3\,r_{\rm eff}$ in the data of NGC 4807. Projected density distortions progressively strengthen in deprojection from $i = 90^\circ$ to $i = 0^\circ$ and assuming $i = 50^\circ$ already causes a considerable amplification. Near the centre – where the observed isophotes are consistent with being purely elliptical – the discy deprojection appears smoother with on average larger a_4, albeit lacking the strong a_4 peak occurring in the deprojection without shape preference at $R = 0.05\,r_{\rm eff}$.

We have constructed orbit models for both the $i = 90^\circ$ and the non-discy $i = 50^\circ$ deprojections, but the heavily distorted density distributions at $i = 50^\circ$ lead us to expect that we likely view NGC 4807 close to edge-on.

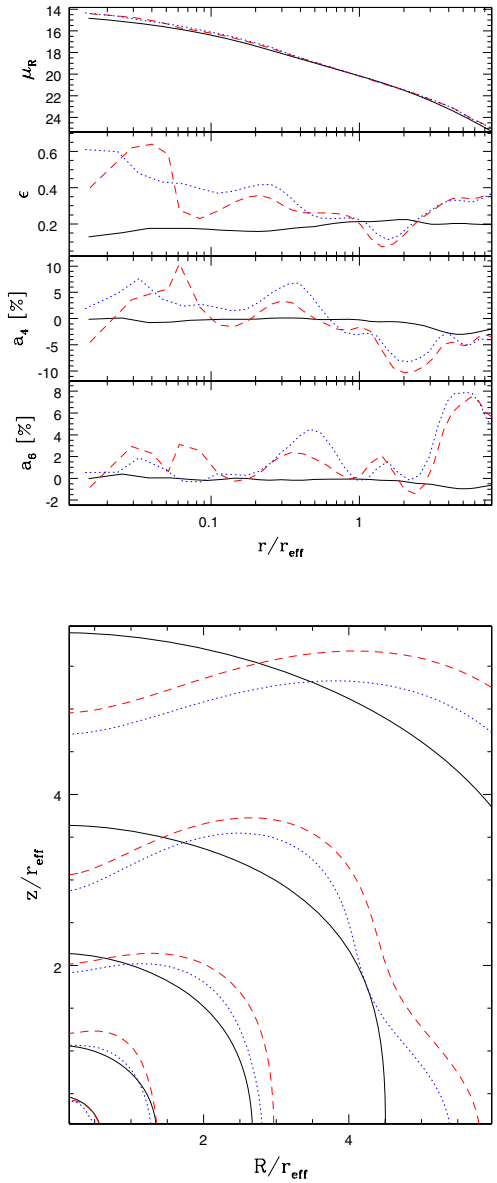

Figure 2. Projected appearance of the three deprojections shown in Fig. 1 when seen edge-on. The top panel shows isophotal shape parameters (cf. Fig. 1), the bottom panel displays the corresponding isophotes. Solid: $i = 90^\circ$ deprojection; dashed: $i = 50^\circ$ deprojection; dotted: discy $i = 50^\circ$ deprojection.

2.3 Kinematic data

The kinematic data are described in Mehlert et al. (2000) and Wegner et al. (2002). They consist of two long-slit spectra for the major and the minor axis, respectively. Profiles of lower order Gauss–Hermite coefficients γ_0, v, σ, H_3 and H_4 (Gerhard 1993; van der Marel & Franx 1993) parametrizing the line-of-sight velocity distribution (LOSVD) reach out to $3\,r_{\rm eff}$ along the major axis and out to $0.6\,r_{\rm eff}$ along the minor axis. Our orbit models are not directly fitted to the observed Gauss–Hermite parameters, but to binned LOSVDs. Therefore the Gauss–Hermite parameters are transformed into suitable LOSVDs as follows. First, the Gauss–Hermite series according to the observed γ_0, v, σ, H_3 and H_4 is evaluated at 1000 values of line-of-sight velocity $v_{\rm los}$, linearly spaced in the range $-4\,\sigma \leqslant v_{\rm los} \leqslant 4\,\sigma$. At each of the sampled projected velocities error bars ΔLOSVD are assigned to the LOSVD from the errors in the corresponding Gauss–Hermite parameters by means of Monte Carlo simulations. The LOSVD is then binned appropriately for comparison with the orbit library (see Section 3.1 below).

For NGC 4807, the scatter in kinematical data from different sides of the galaxy is mostly negligible compared with the statistical errors in the data. Therefore, the orbit models are fitted to a symmetrized data set, derived by averaging the Gauss–Hermite parameters from each side. The largest scatter appears in the outermost major-axis H_4 measurement. To infer the impact of its uncertainty on the reconstructed DF, we separately refitted the mass model that most closely matches the symmetrized data set, to the kinematics of the two different sides of NGC 4807. Both fits lead to similar models in

terms of DF and internal kinematical structure, suggesting that the asymmetry in this single measurement does not largely affect our results.

3 ORBIT SUPERPOSITION MODELS

Our method of setting up orbit libraries to construct best-fitting models is described in detail in Richstone et al. (in preparation) and in Thomas et al. (2004). Here, we only briefly outline some aspects of the method relevant to the present paper.

To recover the mass distribution of a given galaxy by orbit libraries, a grid of (parametrized) trial potentials is probed. In each trial potential (Section 3.2) a large set of orbits is calculated (Section 3.3) and an orbit superposition is constructed that best matches the observational constraints (Section 3.4). The best-fitting mass parameters with corresponding errors then follow from a χ^2-analysis.

3.1 Basic grids

For comparison with observations the meridional plane of the orbit model as well as its projection on to the plane of the sky are divided into bins in radius r and polar angle ϑ. The grid in radius is logarithmic in the outer parts and becomes linear in the inner parts; the angular bins cover equal steps in $\sin\vartheta$ (see Richstone et al., in preparation, for details). For NGC 4807 the models are calculated in $N_r \times N_\vartheta = 200$ bins with $N_r = 20$ and $N_\vartheta = 10$. Each spatial bin of the sky-projection of the model is subdivided into $N_{\rm vel} = 15$ bins in projected velocity for the purpose of fitting the library to the observed kinematics.

3.2 Luminous and dark mass distributions

3.2.1 Luminous matter

We assume that the luminous mass of NGC 4807 is sufficiently characterized by a constant stellar mass-to-light ratio Υ (see also Section 9 and Fig. 22, below, for a verification of this assumption). The stellar mass density then reads $\Upsilon\,\nu$, where the luminosity density ν is taken from the deprojections of Section 2.2.

3.2.2 Dark matter

Modelling of spiral and dwarf galaxy rotation curves indicates shallow inner dark matter density distributions, i.e. logarithmic density slopes $\gamma \equiv \mathrm{d}\ln(\rho_{\rm DM})/\mathrm{d}\ln(r) \approx 0$ (e.g. de Blok et al. 2001; Gentile et al. 2004). Flat dark matter density cores also fit to the kinematics of round ellipticals (Gerhard et al. 2001), although Rix et al. (1997) found steeper profiles consistent with observations of NGC 2434. Some optical or radio rotation curves also allow density slopes up to $\gamma \leqslant -1$, but they do not prefer steep profiles (Swaters et al. 2003).

Shallow dark matter density profiles conflict with predictions of (pure dark matter) cosmological N-body simulations. In the ΛCDM scenario, dark matter distributions with central density cusps around $-1.5 < \gamma < -1$ are found (e.g. Moore et al. 1999; Navarro et al. 2004). Similar steep profiles emerge in warm dark matter (Colin, Avila-Reese & Valenzuela 2000; Knebe et al. 2002), whereas self-interacting dark matter offers central $\gamma \approx 0$ (Davé et al. 2001).

To probe the whole diversity of theoretically and observationally motivated profiles we allow for two different dark matter distributions, one with central $\gamma = 0$, representative of shallow profiles and another with central $\gamma = -1$, representative of the steeper cases.

Cored profiles. A dark matter distribution that provides asymptotically flat circular velocity curves in combination with flat ($\gamma = 0$) inner density cores is given by the logarithmic potential (Binney & Tremaine 1987)

$$\Phi_{\rm LOG}(R, z) = \frac{v_c^2}{2} \ln\left(r_c^2 + R^2 + \frac{z^2}{q^2}\right), \tag{1}$$

where $R = r\cos(\vartheta)$, $z = r\sin(\vartheta)$ are cartesian coordinates in the meridional plane and $\vartheta = 0^\circ$ corresponds to the equator. The density distribution generating $\Phi_{\rm LOG}$ reads (Binney & Tremaine 1987)

$$\rho_{\rm LOG}(R, z) \propto v_c^2 \frac{(2q^2+1)r_c^2 + R^2 + 2(1 - 1/2q^2)z^2}{\left(r_c^2 + R^2 + z^2/q^2\right)^2 q^2} \tag{2}$$

and is positive everywhere for $q \in [1/\sqrt{2}, 1]$. The flattening of the density distribution (2) differs from that of the potential, q. It is generally smaller and varies with radius. In the following, we will only consider cored profiles with $q = 1.0$ (spherical). Together with the assumption of a constant mass-to-light ratio Υ, models with dark matter distributions according to equation (2) can be seen as analogues to maximum-disc models of spiral galaxies and have been called maximum-stellar-mass models (Gerhard et al. 1998).

Cuspy profiles. A representative cuspy mass distribution fitting simulated dark matter haloes over a wide range of radii is the Navarro–Frenk–White (NFW) profile (Navarro et al. 1996)

$$\rho_{\rm NFW}(r, r_s, c) \propto \frac{\delta_c}{(r/r_s)/(1 + r/r_s)^2}, \tag{3}$$

with a central logarithmic density slope $\gamma = -1$. The parameter δ_c in equation (3) is related to a concentration parameter c via

$$\delta_c = \frac{200}{3} \frac{c^3}{\ln(1+c) - c/(1+c)}. \tag{4}$$

By the substitution $r \to r\sqrt{\cos^2(\vartheta) + \sin^2(\vartheta)/q^2}$ equation (3) provides haloes with a constant flattening q.

In CDM cosmology the two parameters c and r_s turn out to be correlated in the sense that higher mass haloes are less concentrated, with some scatter due to different mass assembly histories (Navarro et al. 1996; Jing & Suto 2000; Wechsler et al. 2002). The corresponding relation reads

$$r_s^3 \propto 10^{(A - \log c)/B} \left(200\,\frac{4\pi}{3}\,c^3\right)^{-1}. \tag{5}$$

Here, we take $A = 1.05$ and $B = 0.15$ (Navarro et al. 1996; Rix et al. 1997), which – for the concentrations $5 < c < 25$ considered here – is equivalent to within 10 per cent to the relation given in Wechsler et al. (2002) for the now standard ΛCDM.

3.2.3 Total gravitating mass and potential

Luminous and dark matter components combine to give the total mass density

$$\rho = \Upsilon\,\nu + \rho_{\rm DM}, \tag{6}$$

with $\rho_{\rm DM}$ being either $\rho_{\rm LOG}$ or $\rho_{\rm NFW}$. The potential Φ follows by integrating Poisson's equation.

3.3 Orbit collection

Given Φ, a large set of orbits is calculated in order to sample the phase space of the potential. Energies E and angular momenta L_z of the orbits are chosen to connect every pair of equatorial radial grid

bins by at least one equatorial orbit. The surfaces of section (SOS) connected to pairs of (E, L_z) – here the upward orbital crossings with the equator – are densely filled with orbits of all available shapes (Thomas et al. 2004). A typical orbit library contains between 6500 and 9500 orbits for $L_z > 0$. The retrograde counterpart of each orbit with $L_z < 0$ is included in the library by reversing the azimuthal velocities appropriately. In total a typical library then contains between 13 000 and 19 000 orbits.

3.4 Orbit superposition

Any superposition of the orbits of a library generates a model with a specific internal density distribution and specific projected kinematics that can be compared with the observations. The relative contribution of each orbit to the superposition – the orbital weight w_i – represents the total amount of light carried by orbit i. To fit a library to a given data set the maximum entropy technique of Richstone & Tremaine (1988) is applied by maximizing

$$\hat{S} \equiv S - \alpha\, \chi^2_{\rm LOSVD}, \tag{7}$$

where

$$\chi^2_{\rm LOSVD} \equiv \sum_{j=1}^{N_{\mathcal{L}}} \sum_{k=1}^{N_{\rm vel}} \left(\frac{\mathcal{L}^{jk}_{\rm mod} - \mathcal{L}^{jk}_{\rm dat}}{\Delta \mathcal{L}^{jk}_{\rm dat}} \right)^2 \tag{8}$$

quantifies the deviations between the model LOSVDs $\mathcal{L}_{\rm mod}$ and the observed LOSVDs $\mathcal{L}_{\rm dat}$ at $N_{\mathcal{L}}$ spatial positions j and in the $N_{\rm vel}$ bins of projected velocity k. By S, the Boltzmann entropy

$$S \equiv \int f \ln(f)\, {\rm d}^3 r\, {\rm d}^3 v = \sum_i w_i \ln\left(\frac{w_i}{V_i}\right) \tag{9}$$

of the library's DF f is denoted, V_i is the orbital phase volume of orbit i, computed as in Thomas et al. (2004), and α is a regularization parameter (see Section 4).

The decomposition of the library potential Φ into two components generated by the stellar and the dark matter mass distributions, respectively, is meaningful only if the final orbit model self-consistently generates the stellar contribution to the potential. Therefore, the luminosity density ν is used as a boundary condition for the maximization of equation (7). This also guarantees a perfect match of the orbit model to the photometric observations.

3.5 Comparing model with data kinematics

Since our original data set for NGC 4807 consists of Gauss–Hermite parameters up to H_4 we will quote the deviations between model and data kinematics in terms of

$$\chi^2_{\rm GH} \equiv \sum_{j=1}^{N_{\mathcal{L}}} \left[\left(\frac{v^j_{\rm mod} - v^j_{\rm dat}}{\Delta v^j_{\rm dat}} \right)^2 + \left(\frac{\sigma^j_{\rm mod} - \sigma^j_{\rm dat}}{\Delta \sigma^j_{\rm dat}} \right)^2 + \left(\frac{H^j_{3,\rm mod} - H^j_{3,\rm dat}}{\Delta H^j_{3,\rm dat}} \right)^2 + \left(\frac{H^j_{4,\rm mod} - H^j_{4,\rm dat}}{\Delta H^j_{4,\rm dat}} \right)^2 \right]. \tag{10}$$

The sum in equation (10) over $N_{\mathcal{L}}$ LOSVDs contains $N_{\rm data} \equiv 4 \times N_{\mathcal{L}}$ terms and the parameters $v_{\rm mod}$, $\sigma_{\rm mod}$, $H_{3,\rm mod}$ and $H_{4,\rm mod}$ are obtained from the corresponding LOSVDs of equation (8) by fitting a fourth-order Gauss–Hermite series.[1] Equation (10) can only be applied if the sampling of the LOSVD is sufficient to get reliable and unbiased estimates of the Gauss–Hermite parameters and it should be noticed that in the implementation of the orbit superposition method applied here (in contrast to the programs building up on the work of Rix et al. 1997 and Cretton et al. 1999) $\chi^2_{\rm GH}$ is not explicitly minimized. We discuss the effects of using equation (10) instead of equation (8) to derive confidence regions in Section 9.3.

[1] The fifth parameter of the fit, the intensity γ_0, is not included in equation (10) since we scale data as well as model LOSVDs to the same surface brightness before comparison. This does not automatically imply that the fitted intensities γ_0 of model and data LOSVDs are identical, but it largely affects their differences. Following the approach of Gerhard et al. (1998) we therefore omit γ_0 from $\chi^2_{\rm GH}$.

4 REGULARIZATION

The regularization parameter α in equation (7) controls the relative importance of entropy maximization and χ^2-minimization in the model. Basically, increasing α puts more weight on the χ^2-minimization in the orbit superposition and reduces the influence of S in equation (7). For data sets with relatively sparse spatial sampling as considered here, the freedom in the orbit superpositions allows us to fit models to the noise in the data when applying $\alpha > 1$. Such orbit models show, however, large density depressions and contradict the traditional view of relaxed dynamical systems. On the other hand, models with lower α have smoother distribution functions in the sense that the adopted form for S tends to isotropize the orbital DF, thereby reducing its dependency on L_z and I_3. Fitting orbit models to data sets with different spatial coverage and quality will likely change the effect of α on the final fit. Likewise, changing the functional form of S can be used to bias the models towards other than isotropic DFs (Thomas et al. 2004). The best choice for α and S has to be investigated case-by-case, depending on the galaxies under study and on the amount and form of information that is to be extracted from the observations.

4.1 Motivation

Figs 3 and 4 exemplify the effects of regularization in terms of two distribution functions reconstructed from fits of the same library to an edge-on isotropic rotator model of NGC 4807. The Gauss–Hermite profiles in the lower panels of the figures are derived from velocity moments obeying higher-order Jeans equations in the self-consistent potential of the deprojection (Magorrian & Binney 1994). Before calculating the Gauss–Hermite parameters the velocity moments are slit averaged and seeing convolved to simulate the observations of Section 2.3. Noise is added to v and σ according to the fractional errors of the observations and to H_3 and H_4 according to the absolute errors. The lower panels of Figs 3 and 4, respectively, display the rotator kinematics along the major and minor axes, together with fits of an orbit library containing 2×6922 orbits. For Fig. 3 the fits were obtained at $\alpha = 0.02$ and for Fig. 4 at $\alpha = 6.73$. The distribution functions reconstructed from the two fits are plotted against orbital energy E in the upper panels of the figures. Each dot represents the phase-space density w_i/V_i along a single orbit, scaled according to $\sum w_i = \sum V_i = 1$ (Thomas et al. 2004). The more regularized fit in Fig. 3 yields $\chi^2_{\rm GH}/N_{\rm data} = 0.3$ ($N_{\rm data} = 48$), while for Fig. 4 the goodness of fit is $\chi^2_{\rm GH}/N_{\rm data} = 0.17$.

The DF at $\alpha = 6.73$ has density depressions of several orders of magnitude for orbits with roughly the same energy. Orbit models with such DFs are difficult to interpret as the result of relaxation processes like violent relaxation and others, occurring in the dynamical evolution of real galaxies (e.g. Lynden-Bell 1967). They often predict uncommon kinematics along position angles not covered by observational data. To illustrate this, the projected kinematics predicted along a diagonal axis (position angle $\vartheta = 45°$) by the two DFs of Figs 3 and 4 are plotted in Fig. 5. For comparison the (undisturbed) kinematics of the isotropic rotator model are also overplotted.

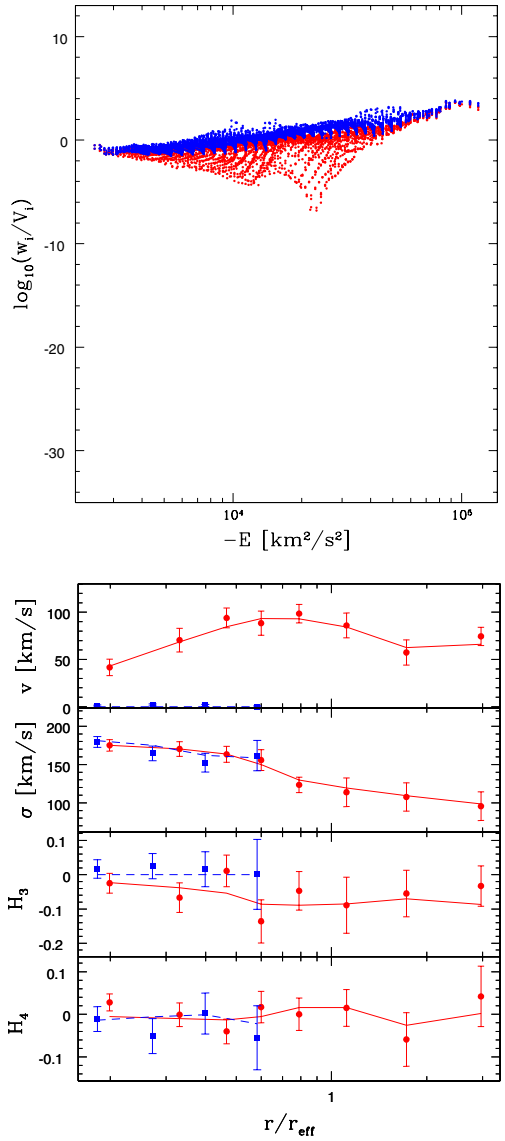

Figure 3. Reconstructed phase-space densities of individual orbits against energy (upper panel) for an isotropic rotator model of NGC 4807 (details in the text). For the underlying fit (lower panel; dots/squares: major/minor axis isotropic rotator model; solid/dashed lines: major/minor axis orbit model) a regularization of $\alpha = 0.02$ is used.

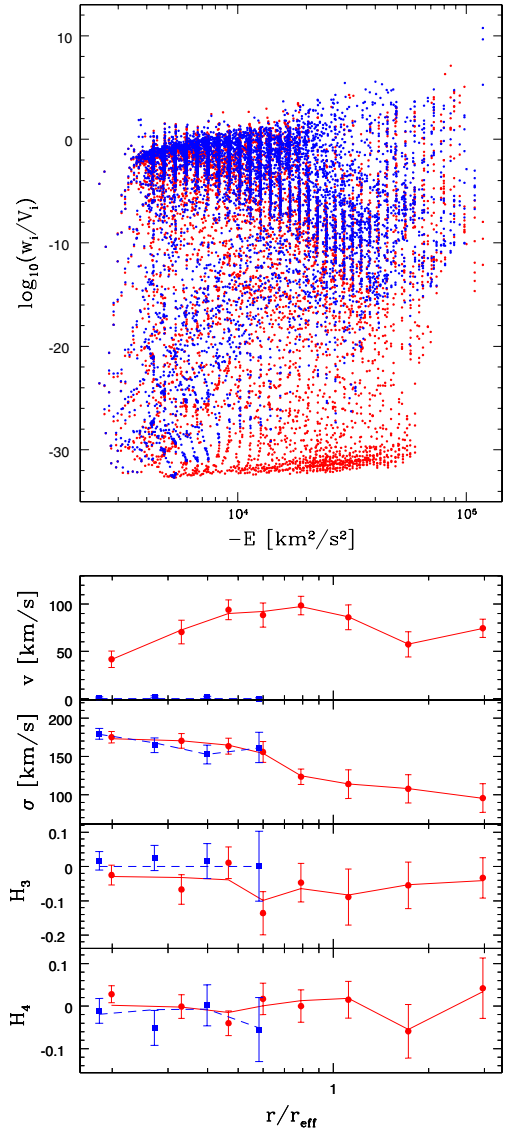

Figure 4. As Fig. 3, but for regularization with $\alpha = 6.73$. Note that the lower boundary of phase-space densities in the upper panel is partly due to the program setting all orbital weights smaller than $w_i < w_{\min} \equiv 10^{-37}$ equal to $w_i \equiv w_{\min}$.

The profiles of the almost non-regularized ($\alpha = 6.73$) fit show large point-to-point variations, which cannot easily be reconciled with the scatter in real observations. Also, the mean deviation between the unregularized orbit superposition and the input isotropic rotator (IR) model are larger for the non-regularized one than for the regularized one, e.g. $\langle H_3^{\rm IR} - H_3 \rangle = 0.06$ for $\alpha = 6.73$ compared with $\langle H_3^{\rm IR} - H_3 \rangle = 0.02$ for $\alpha = 0.02$.

The above example demonstrates the importance of regularization in the context of recovering internal dynamics of isotropic rotators from sparse data sets typical for our sample of Coma galaxies. For NGC 4807 we have determined the optimal amount of regularization by means of Monte Carlo simulations of several such isotropic rotator models (see Section 4.2 below).

The DFs of isotropic rotator models are of the form $f = f(E, L_z)$ and represent only a minority of all possible DFs, since they are constant along I_3. The choice of such reference models for galaxies like NGC 4807 (fast rotating, faint giant ellipticals) is observationally motivated (Kormendy & Bender 1996) and further supported by the weak velocity anisotropy found in previous dynamical studies (e.g. Gerhard et al. 2001; see also Section 7 for the case of NGC 4807), implying only a mild dependence of the DF on I_3. For more luminous ellipticals (shaped primarily by velocity anisotropy) or lenticulars embedded in roundish haloes other reference models should be explored. We will turn to this in a future publication.

4.2 Regularization from isotropic rotator models

The isotropic rotator models constructed to determine the optimal regularization with respect to the analysis of the internal structure of NGC 4807 are based on the edge-on as well as the $i = 50^\circ$ deprojections. For numerical reasons, however, the models for $i = 50^\circ$ are forced to have isophotes close to pure ellipses by setting

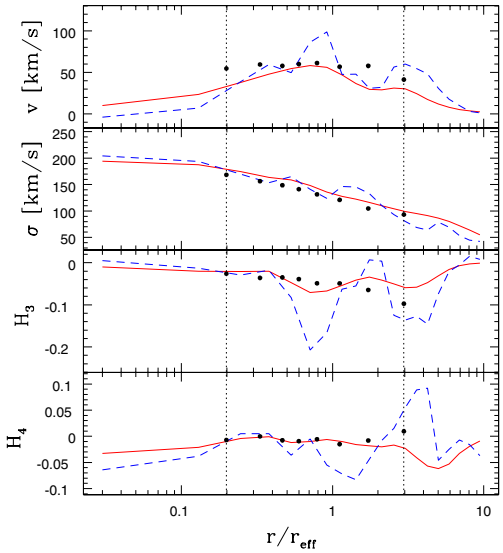

Figure 5. Projected kinematics of the two DFs of Figs 3 and 4 along a diagonal axis with position angle $\vartheta = 45°$. Solid lines: $\alpha = 0.02$ (→ Fig. 3); dashed lines: $\alpha = 6.73$ (→ Fig. 4); dots: kinematics of the isotropic rotator model. Note that the orbit superpositions were fitted to the model only along the major and minor axes.

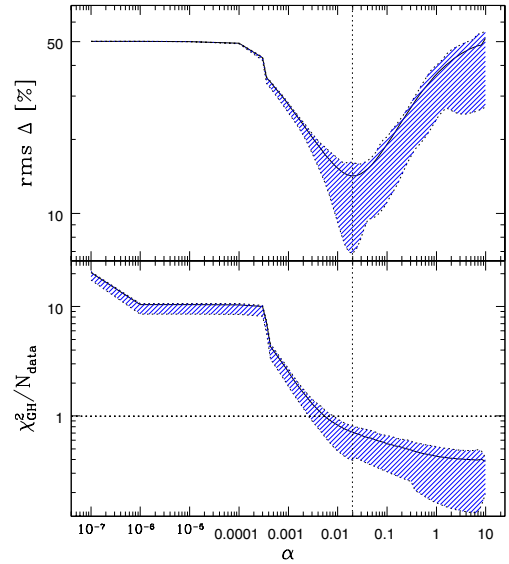

Figure 6. Match $\Delta(\alpha)$ of internal velocity moments and $\chi^2_{\rm GH}/N_{\rm data}$ of the Gauss–Hermite parameters as a function of the regularization parameter α. Lines represent the mean over 60 fits to Monte Carlo realizations of the kinematic profiles of the isotropic rotator; shaded regions encompass 68 per cent of the simulations closest to the corresponding minimum in $\Delta(\alpha)$ and $\chi^2_{\rm GH}/N_{\rm data}$, respectively.

$a_4 \equiv a_6$ for the deprojection. Six models have been probed, three at each of the inclinations $i = 50°, 90°$: one self-consistent, one embedded in a LOG halo and a third embedded in a NFW halo. Kinematic profiles are calculated from higher order internal velocity moments (Magorrian & Binney 1994) following the procedure described in Section 4.1. Orbit libraries are fitted to the kinematic profiles and the internal velocity moments reconstructed from the fits are compared with the original input moments for various values of α. The optimal balance between entropy maximization and χ^2-minimization is revealed where the reconstructed internal velocity moments are closest to the input model.

Fig. 6 shows the results for a self-consistent model based on the $i = 90°$ deprojection. The upper panel shows the rms difference $\Delta(\alpha)$ between original and reconstructed internal velocity moments (up to second order) as a function of the regularization parameter α. The rms is evaluated between the innermost and outermost fitted data points, at all position angles ϑ, including intermediate ones, not covered by data points. The lower panel illustrates the goodness of fit $\chi^2_{\rm GH}/N_{\rm data}$. Solid lines correspond to the mean obtained by fitting orbit models to 60 Monte Carlo realizations of the simulated data. Shaded areas comprise the 68 per cent fraction of best reconstructions (upper panel) and 68 per cent fraction of best-fitting solutions (lower panel), respectively.

The best results are obtained for $\alpha = 0.02$, when internal kinematics of the fits follow the input moments to an accuracy of about 15 per cent in the mean. Lower α yield less accurate reconstructions since the orbit superpositions do not fit the data enough (see $\chi^2_{\rm GH}$ in the lower panel). For larger α on the other hand, the rms $\Delta(\alpha)$ increases, because the library starts to fit the noise in the data.

On average, the orbit models for $\alpha = 0.02$ fit with $\chi^2_{\rm GH}/N_{\rm data} < 1$. A proper normalization for $\chi^2_{\rm GH}$ is, however, hard to obtain, since we do not exactly know the number of free parameters in the library. For $\alpha = 0$ this number is zero, because χ^2 does not appear in equation (7) while for $\alpha \to \infty$ there are roughly as many free parameters as orbits in the library,[2] because then S becomes negligible in equation (7). Thus, we do not try to calculate a reduced χ^2.

Table 1. Summary of simulations aimed at optimizing the regularization parameter α. Columns from left to right: inclination of reference model; potential of reference model (SC = self-consistent, LOG = logarithmic spherical halo, NFW = spherical NFW halo, details in the text); regularization parameter α_0 that yields the best reconstruction of internal velocity moments; rms $\Delta(\alpha_0)$ between internal velocity moments of reference models and reconstructions achieved with $\alpha = \alpha_0$; goodness of fit $\chi^2_{\rm GH}(\alpha_0)$; number of orbits $N_{\rm orbit}$ used for the modelling.

Input model	α_0	$\Delta(\alpha_0)$	$\chi^2_{\rm GH}$ (α_0)	$N_{\rm orbit}$
$i = 90°$, SC	0.0199	13.5 per cent	0.712	2×6922
$i = 90°$, LOG	0.0166	12.7 per cent	0.719	2×8273
$i = 90°$, NFW	0.0138	13.2 per cent	0.692	2×8469
$i = 50°$, SC	0.0238	12.6 per cent	0.539	2×6697
$i = 50°$, LOG	0.0166	13.8 per cent	0.826	2×8126
$i = 50°$, NFW	0.0166	13.5 per cent	0.797	2×8324

Table 1 summarizes the total of simulations done to fix α. The first column labels the three models investigated at each of the two inclinations $i = 50°$ and $i = 90°$ (SC: self-consistent models without halo; LOG: a dark halo with $r_c = 5$ kpc and $v_c = 265\,{\rm km\,s^{-1}}$ according to equation (2) is added to the stars; NFW: dark halo profile like in equation (3) with $r_s = 10.0$ kpc, $c = 27.0$; for all models $\Upsilon = 3.0$). The halo models are constructed to produce a roughly flat circular velocity. In the second column of Table 1 the regularization α_0 is quoted attaining the best reconstruction of the internal velocity moments, quantified in the third column as

[2] We have neglected the boundary condition related to ν. This is expected to reduce the number of free parameters, but is unlikely to break its dependency on α.

$\Delta(\alpha_0) = \min(\Delta(\alpha))$. The corresponding goodness of fit $\chi^2_{\rm GH}(\alpha_0)$ is given in the fourth column of the table. The number of orbits in each of the fitted libraries is found in the last column.

On average, the six probed models yield $\langle\alpha_0\rangle = 0.0179 \pm 0.0035$. The low scatter seems to indicate that α_0 does not depend strongly on the potentials tested. In the implementation of the maximum entropy technique used here, α is increased iteratively in discrete steps (see Richstone et al., in preparation). For the models of NGC 4807 we apply $\alpha = 0.0199 \approx 0.02$, which is the closest larger neighbour of $\langle\alpha_0\rangle$ in these iterations.

In the remainder of the paper, by quoting 68 (90, 95) per cent confidence levels, we always refer to all orbit models whose $\chi^2_{\rm GH}/N_{\rm data}$ are below the corresponding maximum χ^2-level of the 68 (90, 95) per cent best-matching fits in the simulations. For these fits parameters like Υ, i, r_c, v_c, etc. are set equal to the true input values, but in the analysis of real galaxies they are varied. Strictly speaking then, the χ^2-statistics from the simulations are not directly applicable to real galaxies. For example, to determine the correct statistics for the case where Υ, r_c and v_c are varied to find the best-fitting mass model, about 10^2 orbital fits for each triple of (Υ, r_c, v_c) are necessary to yield the corresponding three-dimensional χ^2-distribution. Such simulations, however, cannot be performed in a reasonable amount of time with present-day computer power.

Probably, our confidence regions derived as described above overestimate the error budget. For example, in the simulations we find 68 per cent of all orbits within $\Delta\chi^2_{\rm GH}/N_{\rm data} = 0.38$ from the mean best-fit values. In contrast, applying classical $\Delta\chi^2$-statistics for a two-parameter fit yields about 95 per cent confidence at the same $\Delta\chi^2_{\rm GH}/N_{\rm data} = 0.38$.

5 RECOVERING ISOTROPIC ROTATOR MODELS

The aim of this section is to quantify in a practical sense to what degree a sparse data set like the one described in Section 2.3 constrains the internal kinematics and mass structure of a typical galaxy in our sample.

5.1 Mass-to-light ratio Υ and inclination i

First, we disregard the possible presence of a dark halo and try to recover the mass-to-light ratio and inclination of the self-consistent edge-on model in Table 1. Therefore, Fig. 7 summarizes the results of fitting libraries with mass-to-light ratios in the range $2.0 \leqslant \Upsilon \leqslant 4.0$ and inclinations $i = 50^\circ, 70^\circ, 90^\circ$ to the kinematics of this isotropic rotator model. The goodness of fit $\chi^2_{\rm GH}/N_{\rm data}$ for each pair (Υ, i) is averaged over 10 Monte Carlo realizations of the kinematic profiles and evaluated at two different regularizations. For the upper panel $\alpha = 0.02$ according to the simulations described in Section 4.2. Horizontal dotted lines in the plot correspond to 68, 90 and 95 per cent confidence levels as derived from the statistics of the simulations in Section 4.2.

One can read from the plot that the mass-to-light ratio is well recovered: the orbital fits reveal $\Upsilon = 3.0 \pm 0.5$, where the input model has $\Upsilon_{\rm IR} = 3.0$. The minimum $\chi^2_{\rm GH}$ occurs at the true value independent of the assumed inclination. The latter is only weakly constrained. For $\Upsilon = 3.0$ an inclination of $i = 70^\circ$ results in nearly the same $\chi^2_{\rm GH}/N_{\rm data}$ as the fit with the input $i_{\rm IR} = 90^\circ$. Even the orbit models with $i = 50^\circ$ can only be rejected with less than 90 per cent confidence.

For the lower panel the fits are evaluated at $\alpha = 0.44$ (this choice of α is motivated in Section 6). Although at this less restrictive regularization the confidence intervals shrink as compared with $\alpha = 0.02$ the mass-to-light ratio is now less constrained, $\Upsilon = 3.0 \pm 1.0$. The same holds for the inclination: at $\Upsilon = 3.0$ all three probed inclinations are now within the 68 per cent confidence interval.

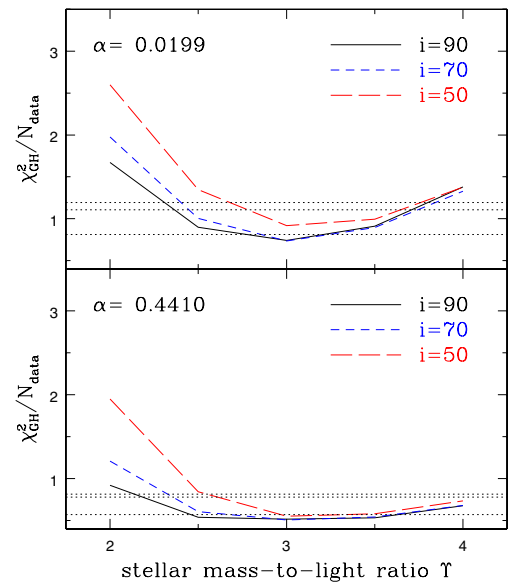

Figure 7. $\chi^2_{\rm GH}$ per data point ($N_{\rm data} = 48$) as a function of stellar M/L for three different inclinations i. Top panel: with optimal smoothing, bottom panel: weak smoothing. The input 2I-model has $M/L = 3.0$ and is edge-on. Pointed horizontal lines in each panel represent the $\chi^2_{\rm GH}$ values enclosing 68, 90 and 95 per cent of the Monte Carlo simulations, respectively.

5.2 Internal kinematics

To give an impression of the ability to recover internal motions (assuming the potential is known) Fig. 8 compares internal velocity moments reconstructed from libraries fitted to the self-consistent

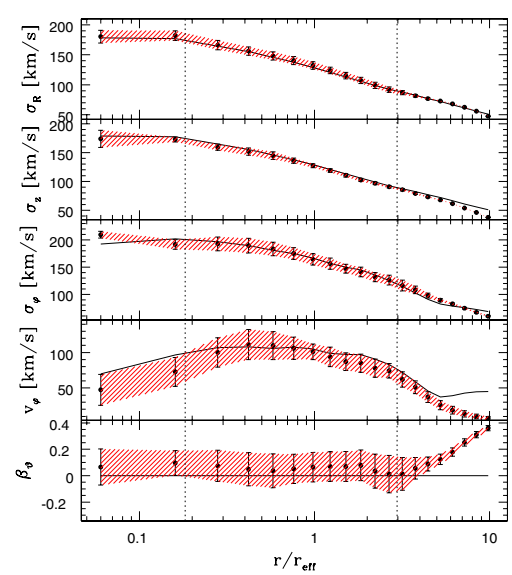

Figure 8. Internal velocity moments along the major axis of libraries fitted to the self-consistent edge-on isotropic rotator model of Section 4.1. Dots: mean from fits to 60 Monte Carlo realizations of the kinematic data; shaded regions: 1σ deviation from the mean; solid lines: velocity moments of the input model; dotted lines: boundaries of the radial region included in the fit.

edge-on isotropic rotator model of Section 4.1 with the corresponding moments of the input model. Solid lines portray the isotropic rotator model and points show the average reconstructed moments from fits to 60 Monte Carlo simulations of the kinematic profiles; error bars indicate 1σ deviations from the mean. For the reconstructions $\alpha = 0.02$ is used.

The three upper rows demonstrate that for the internal major axis the second-order moments σ_R, σ_z and σ_φ are accurately reproduced by the fit over the region between the dotted vertical lines indicating the radii of the innermost and outermost kinematical points included in the fit. The fractional errors of σ_R and σ_φ are below 3 per cent and of σ_z are below 6 per cent. For the internal rotation velocity v_φ the fractional errors are larger than 10 per cent at some points. The match of the rotation velocity can be increased when going to larger α, but then the second-order moments start to wiggle around the input moments and the overall match of reconstructed to original moments becomes worse. Fig. 8 is representative also of the remaining internal position angles of the libraries. It follows that most of the rms in Fig. 6 results from a mismatch in v_φ.

The last row shows a comparison of the anisotropy parameter $\beta_\vartheta = 1 - \sigma_\vartheta^2/\sigma_r^2$, which vanishes for isotropic rotator distribution functions $f = f(E, L_z)$. The reconstructions are consistent with $\beta_\vartheta = 0$ given the scatter caused by the noisy data. The small offset of $\Delta\beta_\vartheta = 0.05$ is due to a slight overestimation of the radial velocity dispersion and emphasizes how sensitive β_ϑ responds to small inaccuracies in the velocity dispersions.

5.3 Mass distribution

The next step is to recover the structure of the isotropic rotator model in the second row of Table 1, where a logarithmic dark halo is present. To this end, we fitted libraries with different dark haloes to pseudo-data-sets of the rotator model, keeping the stellar mass-to-light ratio constant. Fig. 9 combines the results of the simulations. It shows, from top to bottom, cumulative mass-to-light ratio $M(r)/L(r)$, circular velocity $v_{\rm circ}(r)$ and dark matter fraction $M_{\rm DM}(r)/M(r)$ as a function of radius. Vertical dotted lines mark the boundaries of the spatial region covered with kinematic data, thick lines display the input model. The shaded areas have been constructed by determining at each radius the minimum and maximum of M/L, $v_{\rm circ}$ and $M_{\rm DM}/M$ of all libraries within the 68 per cent confidence range derived from the simulations of Section 4.2. Libraries with LOG haloes as well as NFW haloes have been tried (see below) and for each library fits to 10 realizations of the isotropic rotator kinematics were averaged.

The figure demonstrates that in the region covered by the data the mass structure of the input model is well reproduced, with progressively larger scatter towards the outer edge of the data. The uncertainty of the mass-to-light ratio is $\Delta M/L \approx 1.0$ at $1\,r_{\rm eff}$, and the circular velocity is accurate to 10 per cent at the same central distance. In the outer parts orbit superpositions with larger masses than the input model are more consistent with the data than smaller mass models. Nevertheless, the dark matter fraction is determined to $\Delta(M_{\rm DM}/M) = 0.2$ even at the outermost data point.

The top panel of Fig. 10 displays 68, 90 and 95 per cent confidence intervals for the two parameters r_c and v_c of LOG haloes (cf. equation 2). Each dot marks a pair of (r_c, v_c) probed by fitting a library to 10 realizations of the pseudo-data as described above. The dark halo parameters of the input model are marked by the asterisk; the circle designates the best-fitting orbit model.

As expected, the halo parameters are not well constrained. Although the best-fitting parameter pair is close to the input model, the 68 per cent confidence contour comprises a large set of libraries and remains open to the upper right edge of the plot. This follows from a degeneracy between the two parameters r_c and v_c (e.g. Gerhard et al. 1998). Increasing r_c and v_c appropriately puts more mass in the outer parts of the haloes while rendering the regions covered by kinematics roughly unchanged. The increasing width of the shaded areas in the upper two panels of Fig. 9 is an illustration of this degeneracy.

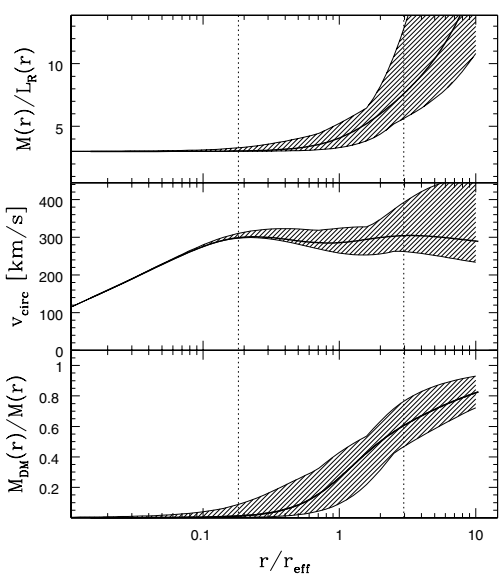

Figure 9. Accuracy of the mass reconstruction. Thick lines: the isotropic rotator model marked by the asterisk in Fig. 10; shaded areas: 68 per cent confidence regions of fits to pseudo-data-sets of the model. For each mass model the goodness of fit is averaged over 10 fits to MC realizations of pseudo-data.

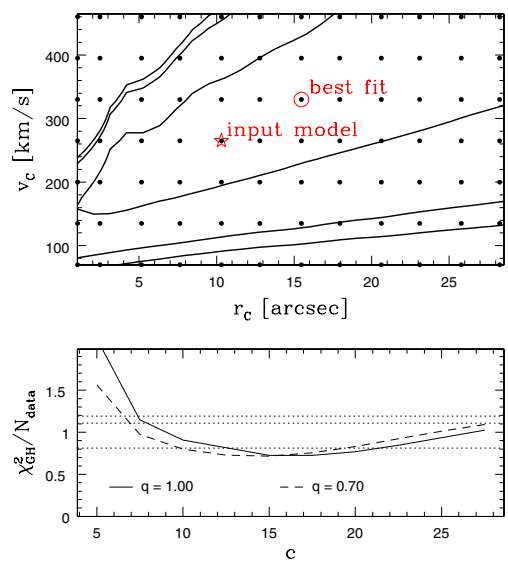

Figure 10. Recovering the dark halo of an isotropic rotator model: r_c and v_c of the input model model are marked by the asterisk in the top panel, the best-fitting reconstruction is marked by the circle. Lines in the top panel display 68, 90 and 95 per cent confidence contours of the fits. The lower panel shows – for the same input model – χ^2 of NFW-type fits (solid/dashed: $q = 1.0/q = 0.7$); horizontal lines: 68, 90 and 95 per cent confidence levels. Each library has been fitted to 10 realizations of the input-model kinematics.

We also fitted one-parameter NFW haloes according to equation (5) to the same isotropic rotator model in order to examine whether these profiles can be excluded by the data set at hand. The lower panel of Fig. 10 displays the results in terms of $\chi^2_{\rm GH}/N_{\rm data}$ as a function of concentration index c. Horizontal dotted lines correspond to 68, 90 and 95 per cent confidence levels; the solid line shows fits with spherical haloes ($q = 1.0$), while for the dashed line $q = 0.7$. Apparently, neither the halo flattening nor the central halo density slope are constrained by the data, because both spherical as well as flattened NFW haloes exist that provide fits equally as good as the LOG haloes. These NFW haloes join smoothly to the mass distribution recovered in Fig. 9 and mimic LOG haloes over the limited spatial region covered by kinematic data.

Fig. 10 suggests that it is not possible to discriminate between LOG and NFW haloes insofar as they provide similar mass distributions over the spatial region sampled by kinematic data. More extended data sets are likely to reduce this degeneracy, but will probably not completely remove it. On the other hand, as Fig. 9 reveals, the mass distribution and composition of the input model can be recovered well, independently of the specific parametrization chosen to emulate it.

6 DARK MATTER IN NGC 4807

Now, we turn to the analysis of the distribution of luminous and dark mass in NGC 4807. Fig. 11 shows the minimum $\chi^2_{\rm GH}/N_{\rm data}$ (scaled, see below) for each modelled stellar mass-to-light ratio $\Upsilon \in \{1.0, 2.0, 2.5, 3.0, 3.5, 4.0, 5.0\}$. Horizontal lines indicate the 68, 90 and 95 per cent confidence limits derived from the simulations of Section 4.2. For the upper panel $\alpha = 0.02$ is used and LOG potentials with stellar mass-to-light ratios $2.5 \leqslant \Upsilon \leqslant 3.0$ fit best to the data. Projected kinematics of the best-fitting orbit model are plotted in the upper panel of Fig. 12 together with the data. The model is edge-on, has stellar $\Upsilon = 3.0$ and a spherical dark halo of LOG type with core radius $r_c = 6.8$ kpc and asymptotic circular velocity

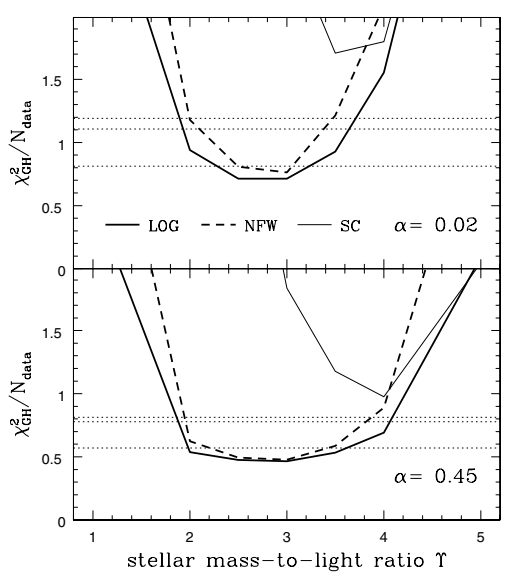

Figure 11. Deviations between the observed kinematics of NGC 4807 and the fitted libraries in terms of $\chi^2_{\rm GH}$ as a function of Υ. At each Υ the minimum min $(\chi^2_{\rm GH})$ is plotted, separately for the case of LOG haloes (thick solid line), one-parameter NFW haloes (thick dashed) and for the self-consistent case (thin solid). For the top row the regularization parameter is $\alpha = 0.02$, for the bottom row $\alpha = 0.45$.

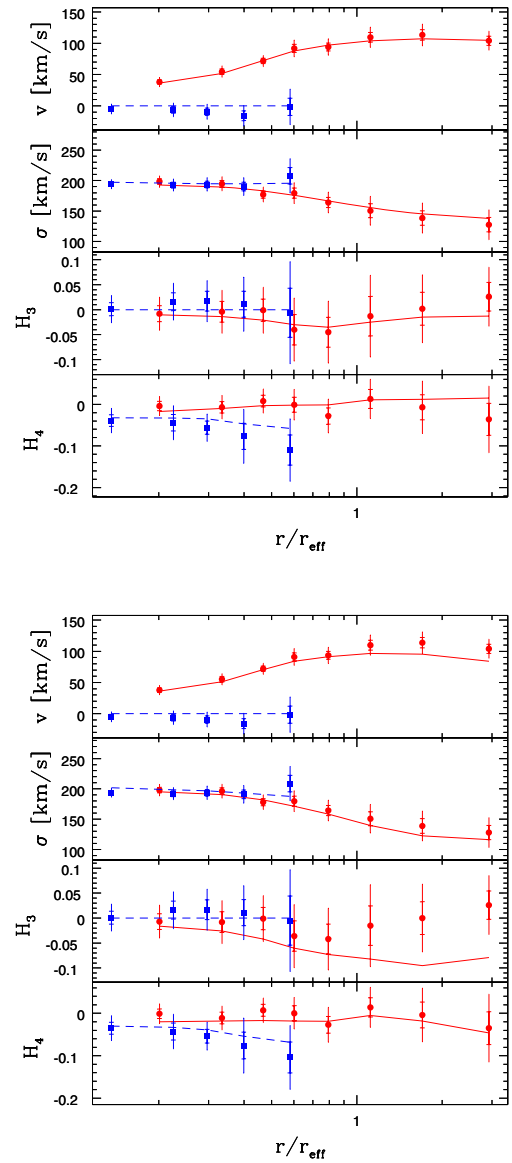

Figure 12. Comparison of NGC 4807 (dots: major axis kinematic data; squares: minor axis) with the overall best-fitting model (upper panel) and best-fitting self-consistent model (lower panel). Both orbit models are at $i = 90°$. For each data point two error bars are given: the statistical error from the observational data (larger, without marks) and the error bar corresponding to the scaled $\chi^2_{\rm GH}$ (marks).

$v_c = 300\,{\rm km\,s^{-1}}$. It fits the data very well with (unscaled) min $(\chi^2_{\rm GH}/N_{\rm data}) = 0.17$, even too well when compared with the average $\langle\chi^2_{\rm GH}/N_{\rm data}\rangle = 0.71$ expected from the Monte Carlo simulations. Since both the scatter in the kinematic data from different sides of the galaxy (cf. Section 2.3) and the point-to-point variations in the profiles are smaller than the statistical error bars, the latter might be slightly overestimated. Hence, in the following all $\chi^2_{\rm GH}/N_{\rm data}$ are rescaled such that min $(\chi^2_{\rm GH}/N_{\rm data}) = \langle\chi^2_{\rm GH}/N_{\rm data}\rangle$. The good match of model and data nevertheless reconfirms that NGC 4807 is consistent with axisymmetry.

Applying regularization with $\alpha = 0.02$, self-consistent models (mass follows light) are ruled out by more than 95 per cent confidence (see the thin solid line in the upper panel of Fig. 11). The best-fitting self-consistent model fits with (rescaled) $\chi^2_{\rm GH}/N_{\rm data} = 1.67$

and is compared with the data in the bottom panel of Fig. 12. It has $\Upsilon = 3.5$, larger than the best-fitting halo model, but fails to reach the measured rotation in the outer parts of the galaxy. A drop in the outer major-axis H_3 profile indicates that the model maintains the measured dispersion σ around the observed v partly by putting light on retrograde orbits. This causes the LOSVD to fall off too sharply at velocities larger than v and to develop a wing at negative velocities, resulting in the too negative H_3. Lack of support for dispersion at large rotation velocities hints at mass missing in the outer parts of this model. Higher mass-to-light ratios, however, would strengthen the mismatch between the central regions of the model and the innermost (minor axis) velocity dispersions.

To push the self-consistent model to the same level of agreement with the data reached in the upper panel of Fig. 12, regularization must be lowered to $\alpha = 0.45$. Although the best-fitting self-consistent model then gives a satisfactory fit in the sense of a reasonable $\chi^2_{\rm GH}/N_{\rm data}$, it is again ruled out by more than 95 per cent confidence when compared with the mean $\langle\chi^2_{\rm GH}/N_{\rm data}\rangle$ using the Monte Carlo simulations, because halo models at $\alpha = 0.45$ still give significantly better fits to the data. The only effect of lower regularization – as shown in the run of $\chi^2_{\rm GH}/N_{\rm data}$ versus Υ in the lower panel of Fig. 11 – is a slight broadening of the minimum region in $\chi^2_{\rm GH}/N_{\rm data}$ and, consequently, an expansion of the allowed range of mass-to-light ratios, yielding now $2.0 \leqslant \Upsilon \leqslant 3.5$ as compared with $2.5 \leqslant \Upsilon \leqslant 3.0$ at $\alpha = 0.02$. Concluding, NGC 4807 cannot be convincingly modelled with self-consistent orbit models, even for weak regularization.

In Fig. 13 (from top to bottom) the 68 per cent confidence regions of cumulative mass-to-light ratio $M(r)/L_R(r)$, circular velocity $v_{\rm circ}$ and dark matter fraction $M_{\rm DM}(r)/M(r)$ are shown (analogue to Fig. 9). Within 1 $r_{\rm eff}$ dark matter is negligible and the dynamical mass-to-light ratio equals the stellar one, $M(r)/L_R(r) = \Upsilon = 3.0$. Between 1 $r_{\rm eff}$ and 3 $r_{\rm eff}$ dark matter comes up from $M_{\rm DM}/M = 0.21 \pm 0.14$ to $M_{\rm DM}/M = 0.63 \pm 0.13$ and combines with the luminous matter to a roughly flat circular velocity curve with $v_{\rm circ} = 280 \pm 30$ km s^{-1} at 1 $r_{\rm eff}$ and $v_{\rm circ} = 318 \pm 48$ km s^{-1} at the last kinematic data point. In the same spatial region the total mass-to-light ratio

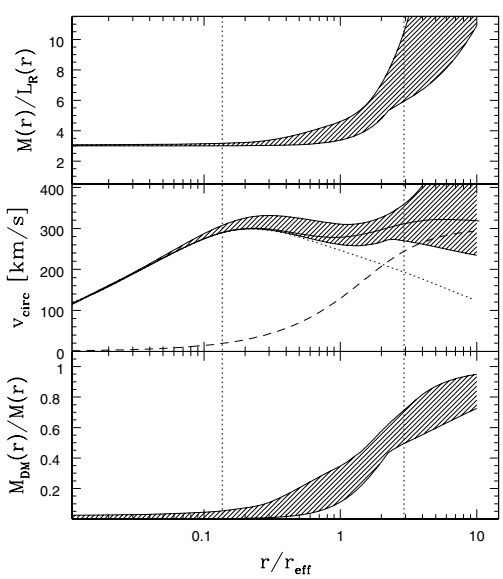

Figure 13. Mass-structure of NGC 4807. Shaded regions are constructed as for Fig. 9. In the middle panel, the circular velocity curve of the best-fitting orbit model (solid line) and its decomposition into the stellar (dotted) and dark matter part (dashed) are displayed.

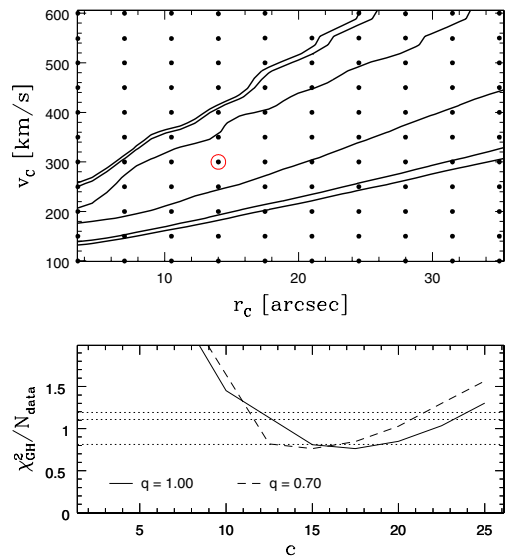

Figure 14. As Fig. 10, but for libraries fitted to the kinematics of NGC 4807. The best-fitting LOG model is designated by the ring. In the lower panel results for spherical (solid line) as well as flattened NFW haloes are illustrated (dashed line: $q = 0.7$).

rises from $M(r)/L_R(r) = 3.8 \pm 0.8$ to $M(r)/L_R(r) = 8.4 \pm 2.4$. Dark mass equals luminous mass at roughly two effective radii. Beyond the last kinematic data point, the models are not well constrained and the profiles start to diverge.

In accordance with the isotropic rotator simulations the halo parameters r_c and v_c are not well constrained – demonstrated by the 68, 90 and 95 per cent confidence contours in Fig. 14. The tilted contour cones are narrower than expected from Fig. 10. Note, however, that we have rescaled the $\chi^2_{\rm GH}$ and hence effectively reduced the error bars as compared with the simulations. Therefore, also the shaded areas in Fig. 13 are smaller than the corresponding areas in Fig. 9.

In the lower panel of Fig. 14 the goodness of fit $\chi^2_{\rm GH}/N_{\rm data}$ is plotted versus concentration c for the one-parameter family of NFW profiles. As in the simulations of Section 5.3, the halo flattening is not constrained and with a best-fitting $\chi^2_{\rm GH}/N_{\rm data} \approx 0.77$ spherical as well as flattened NFW haloes provide almost indistinguishable good fits to the data as the best-fitting LOG haloes. In the innermost regions of those libraries that match the observations, we find $\rho/\rho_{\rm DM} > 10$; the logarithmic density slope of the best-fitting spherical NFW model is $\gamma = -1.8$ at the outermost major-axis data point and $\gamma = -2.41$ at the outer edge of the orbit library. Hence, as already pointed out in Section 5.3, the mass distributions of the data-allowed NFW models – over the modelled spatial region – resemble haloes of LOG type. Fig. 15 illustrates the data-allowed range of dark matter densities along the major axis. Note that the lower limit on $\rho_{\rm DM}$ is likely due to the limited range of profile shapes probed in our study. Dark matter distributions with negative central density slopes $\gamma < 0$ (not tested here) might also provide acceptable orbit models.

Models for $i = 50^\circ$ are ruled out by more than 68, but less than 90 per cent confidence. The best-fitting case is confronted with the kinematic observations in Fig. 16. Representative for all low-inclination models, it fails to reproduce the minor-axis H_4-profile, but the mass structure of this model joins to the profiles in Fig. 13 and the inferred structural properties of the galaxy are robust against the assumed inclination.

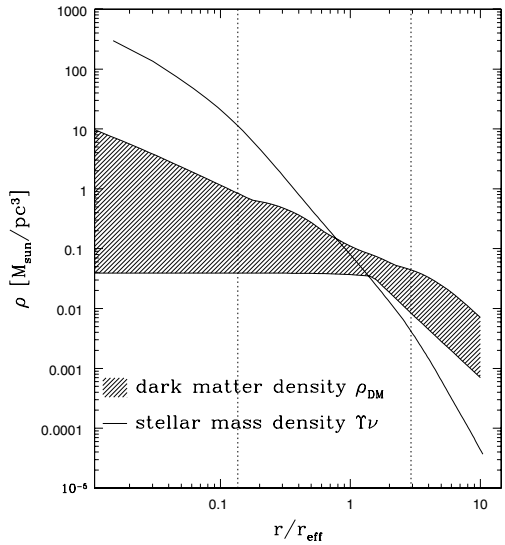

Figure 15. Major-axis stellar mass density according to the edge-on deprojection (solid line, $\Upsilon = 3.0$) and data allowed dark matter densities. Both LOG and NFW haloes are included in the plot. (The shaded area is constructed analogously to Fig. 9.)

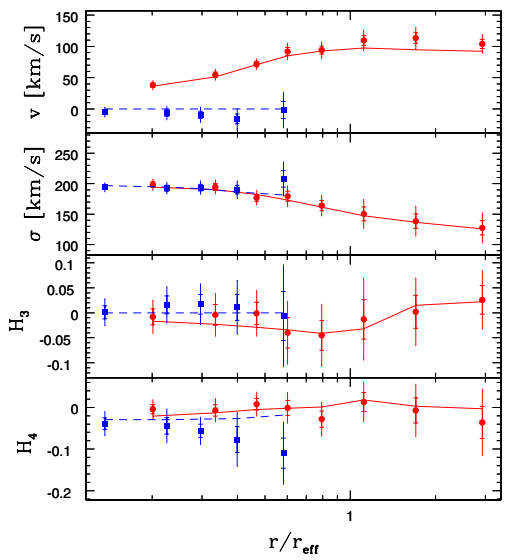

Figure 16. As Fig. 12, but for the best-fitting model at $i = 50°$.

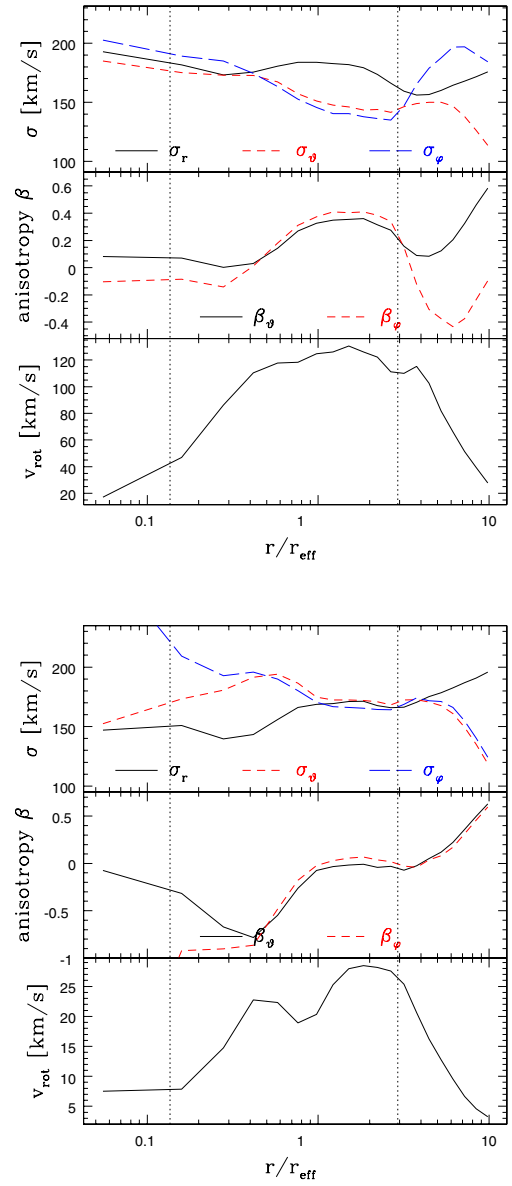

Figure 17. Internal kinematics of the best-fitting halo model near the major axis (top panel; position angle $\vartheta = 2.°9$) and near the minor axis (bottom panel; $\vartheta = 77.°1$), respectively. From top to bottom: velocity dispersions σ_r (solid), σ_ϑ (short-dashed) and σ_φ (long-dashed); velocity anisotropy β_ϑ, β_φ; internal rotational velocity $v_{rot} = v_\varphi$. Vertical, dotted lines indicate the innermost and outermost radius of kinematic data. Note, that the minor axis data reach only out to $0.6\,r_{eff}$.

7 STELLAR MOTIONS IN NGC 4807

Visual inspection of the surfaces of section reveals that none of the orbit libraries for NGC 4807 contains a significant fraction of chaotic orbits. In the best-fitting models, at all inclinations, no indication of chaos is detectable at all.

The internal orbital structure of the best-fitting edge-on halo model near the major and minor axes is shown in Fig. 17. Around the equatorial plane, at radii $1\,r_{eff} < r < 3\,r_{eff}$, the model is characterized by radial anisotropy. Enhanced radial velocity dispersion σ_r causes $\beta_\vartheta \approx \beta_\varphi \approx 0.3$, whereas $\sigma_\vartheta \approx \sigma_\varphi$. Taking the large rotation velocity into account, energy in azimuthal motion turns out to be roughly equal to the energy in radial motion, $\langle v_\varphi^2 \rangle \equiv v_{rot}^2 + \sigma_\varphi^2 \approx \sigma_r^2$. On the other hand, motion perpendicular to the equator is suppressed. Approaching the central parts the velocity structure changes to isotropy and inside $r < 0.5\,r_{eff}$ stays isotropic.

Close to the minor axis, NGC 4807 appears nearly isotropic in the outer parts $1\,r_{eff} < r < 3\,r_{eff}$ with decreasing radial dispersion towards the centre, such that $\beta_\vartheta \approx \beta_\varphi < -0.5$ inside $r < 0.5\,r_{eff}$.

68 per cent confidence intervals analogous to Fig. 9 for velocity anisotropies β_ϑ and β_φ as well as internal rotation velocities near the major and minor axes are shown in Fig. 18. Most tightly constrained is the major-axis rotation, rising from the central parts outwards until settling constant between r_{eff} ($v_{rot} = 124 \pm 6$ km s^{-1}) and $3\,r_{eff}$ ($v_{rot} = 107 \pm 4$ km s^{-1}). Velocity anisotropy is determined to at least $\Delta\beta \leqslant 0.2$ and the trends in the anisotropy structure of

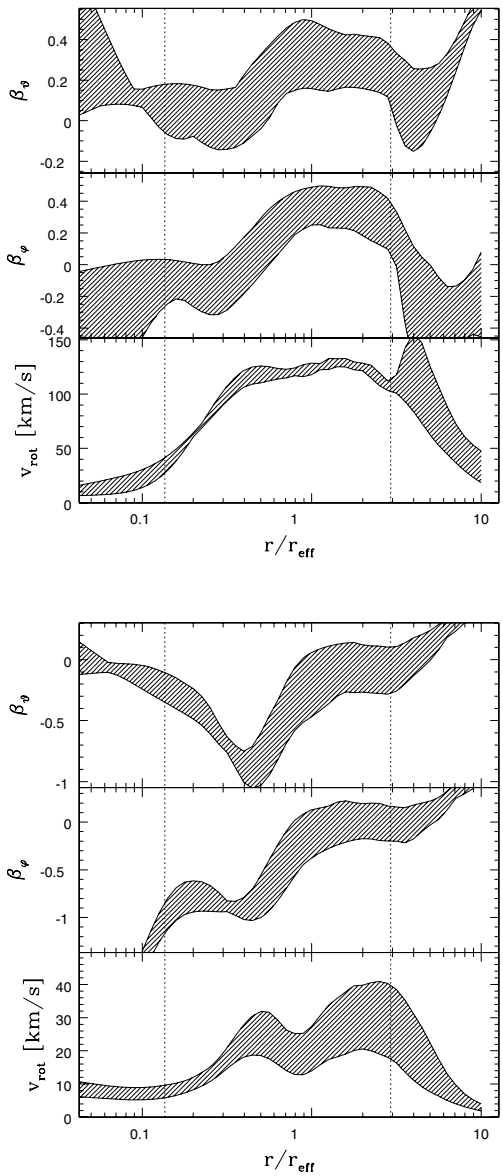

Figure 18. Confidence regions for meridional velocity anisotropy β_ϑ, azimuthal velocity anisotropy β_φ and internal rotational velocity v_{rot} (upper panel: near major axis, position angle $\vartheta = 2\overset{\circ}{.}9$; lower panel: near minor axis, position angle $\vartheta = 77\overset{\circ}{.}1$) of NGC 4807. Shaded areas are constructed as for Fig. 9.

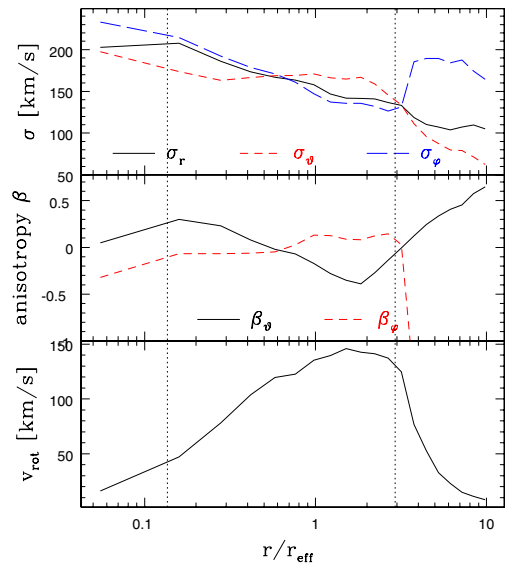

Figure 19. Internal close-to-major axis kinematics (position angle $\vartheta = 2.9^\circ$) of the best-fitting orbit model at $i = 50^\circ$. Line definitions as in Fig. 17.

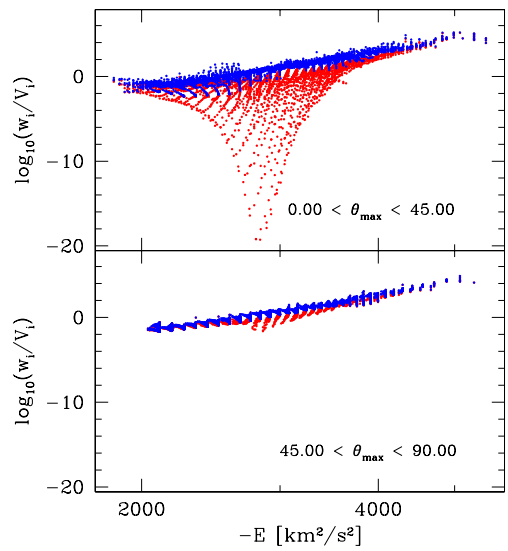

Figure 20. Reconstructed distribution function of the best-fitting orbit model at $\alpha = 0.02$. Each dot represents the phase-space density along a single orbit. Upper row: orbits confined to a konus with opening angle $\vartheta_{max} < 45^\circ$ around the equator; lower row: remaining orbits.

the best-fitting model in Fig. 17 are clearly seen in all allowed orbit models.

Fig. 19 illustrates the internal close-to-major axis kinematics of the best-fitting orbit model at $i = 50^\circ$. In contrast to the edge-on models, $\beta_\vartheta \approx 0$ over almost the whole region constrained by observations, with a slight rise towards the centre. Isotropy in the meridional plane ($\sigma_r \approx \sigma_\vartheta$) is accompanied by suppressed azimuthal dispersion σ_φ. But in contrast to the edge-on model of Fig. 17, the rotation of the actual model causes $\langle v_\varphi^2 \rangle / \sigma_r^2 \approx 1.7$, so that this model is dominated by azimuthal motion near the equatorial plane.

8 PHASE-SPACE STRUCTURE OF NGC 4807

In Fig. 20 phase-space densities w_i/V_i of individual orbits are plotted against orbital energy E for the best-fitting orbit model of NGC 4807. The top panel only includes orbits whose maximally reached latitude, ϑ_{max}, is lower than $\vartheta_{max} < 45^\circ$. These orbits are confined to a cone with opening angle $\vartheta < 45^\circ$ around the equatorial plane. The remaining orbits are plotted separately in the bottom panel. As in Figs 3 and 4 the phase-space densities are scaled according to $\sum w_i = \sum V_i = 1$, where w_i and V_i are the orbital weights and orbital phase volumes, respectively. Whereas the orbits maintaining the bulge of the galaxy follow a DF similar to that shown in Fig. 3, some of the orbits confined around the equatorial plane are strongly depopulated. Around $E \approx 3000\,\mathrm{km^2\,s^{-2}}$ phase-space densities are up to 20 orders of magnitude below the mainstream DF.

In the upper panel of Fig. 21 orbital phase densities are plotted against maximum orbital elongation ϑ_{max} in the meridional plane. The three rows show orbits located in three different spatial

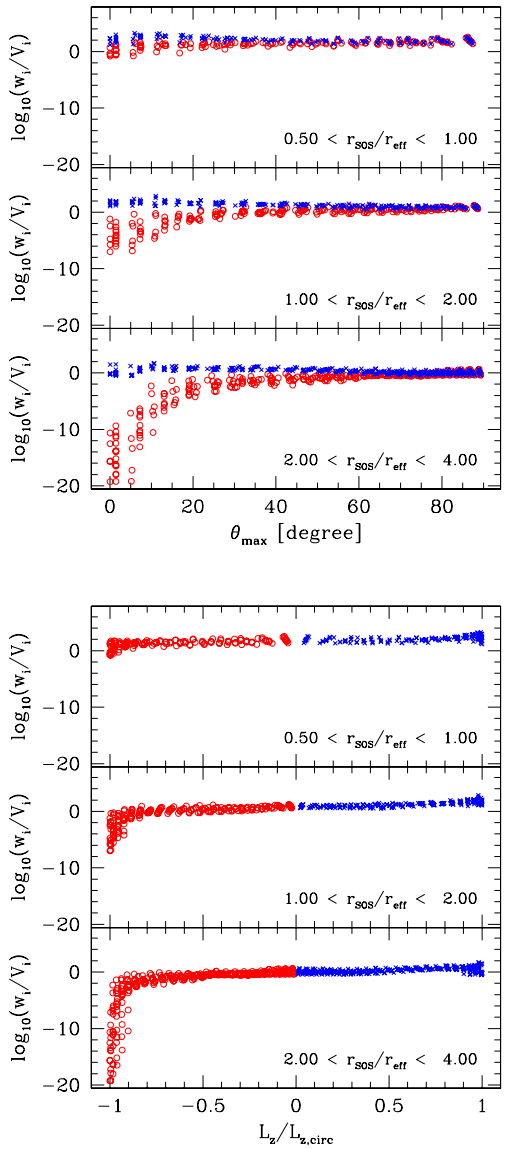

Figure 21. The same model as in Fig. 20. Top panel: phase densities versus maximum orbital elongation $\vartheta_{\max}$ in the meridional plane. Bottom panel: phase densities versus 'circularity' (L_z scaled by the angular momentum $L_{z,\mathrm{circ}}$ of a circular orbit with same energy). Crosses (open circles) denote orbits with positive (negative) L_z. Orbits are extracted from different spatial regions of the model as designated in the panels (see text for details). For each spatial region the number of prograde orbits (crosses) equals the number of retrograde orbits (open circles).

regions separately. The top row includes only orbits whose invariant curves in the surface of section are confined to $0.5\,r_{\mathrm{eff}} < r_{\mathrm{SOS}} < 1\,r_{\mathrm{eff}}$.[3] The spatial regions for the other two rows are $1\,r_{\mathrm{eff}} < r_{\mathrm{SOS}} < 2\,r_{\mathrm{eff}}$ and $2\,r_{\mathrm{eff}} < r_{\mathrm{SOS}} < 4\,r_{\mathrm{eff}}$, respectively. Crosses denote orbits with positive $L_z > 0$ while open circles denote orbits with negative $L_z < 0$. From the centre outwards, orbits with negative angular momentum are progressively depopulated as compared with their counterparts at positive L_z. The difference between prograde and retrograde orbits is most noticeable near the equatorial plane and disappears completely for bulge orbits reaching up to higher latitudes. In the bottom panel of Fig. 21 orbital phase densities are plotted against $L_z/L_{z,\mathrm{circ}}$, $L_{z,\mathrm{circ}}$ being the angular momentum of a circular orbit with the actual energy. Phase-space densities are extracted in the same spatial regions as for the upper panel of the figure. It is now apparent that the keel in the DF of Fig. 20 is caused by a depopulation of (retrograde) circular orbits (at $|L_z| \approx L_{z,\mathrm{circ}}$).

In fact, depopulation of retrograde near-circular orbits leading to the just-described keel appears in all data-allowed DFs, with a slight tendency to be less pronounced in flattened haloes. Even the DFs obtained assuming NGC 4807 is inclined by $i = 50^\circ$ are featured by this structure, albeit there, the keel is not exclusively made of retrograde orbits: also some of the prograde orbits are suppressed. In the low-inclination DFs a third prominent substructure in phase space emerges in the form of a significant fraction of high-energy orbits (around $E \approx -2500\,\mathrm{km^2\,s^{-2}}$) being suppressed by about six orders of magnitude in density, independent of L_z. This structure partly overlays the keel and is caused by the distorted luminosity density at $i = 50^\circ$ since it shows up even in the maximum-entropy models ($\alpha \approx 0$) which are only forced to reproduce the density profile, but not fitted to the kinematics.

Orbits in the keel together with their prograde counterparts (approximately all orbits i with $w_i^+/w_i^- > 99$, where $w_i^\pm \equiv w(E_i, \pm L_{z,i}, I_{3,i})$, $1 \leqslant i \leqslant N_{\mathrm{pro}}$ and N_{pro} prograde orbits in the model) make only 4.3 per cent of the total model. Without these orbits, a slowly rotating bulge ($v \approx 70\,\mathrm{km\,s^{-1}}$ at $r > r_{\mathrm{eff}}$) with a slightly peaked velocity distribution ($H_4 > 0.04$ at $r > r_{\mathrm{eff}}$) appears (see also Section 9.4). On the other hand, the extracted orbits rotate with about $200\,\mathrm{km\,s^{-1}}$ and produce a narrow, low-dispersion LOSVD. They develop a dumbbell-like structure extending to $2\,r_{\mathrm{eff}}$ above the equatorial plane. The fraction of extracted orbits additionally obeying $\vartheta_{\max} < 10^\circ$ shrinks to 0.7 per cent of the total model.

9 SUMMARY AND DISCUSSION

9.1 Regularized orbit models

We have investigated how closely the internal mass distribution and kinematic structure of a galaxy can be recovered from a sparse kinematic data set typical of our project aimed at investigating a sample of flattened early-type galaxies in the Coma cluster. The degree to which orbit models follow internal galaxy properties depends on the amount of regularization applied in the fits. In the maximum-entropy technique of Richstone & Tremaine (1988) used here, a regularization parameter α controls the relative importance of entropy maximization (regularization) on the one hand, and the fit to the data on the other. To find out which choice of α is optimal with respect to our goal of determining galaxy structural parameters, we simulated observationally motivated isotropic rotator models under realistic observational conditions. The models are based on a prototypical elliptical in our sample, NGC 4807. By varying α in the fits of appropriate orbit libraries to pseudo-data of the reference models, the match between internal velocity moments of input model and orbital reconstruction can be evaluated as a function of regularization.

Our simulations indicate that the mass structure of an elliptical can be recovered to about 15 per cent accuracy in terms of the mass-to-light ratio and circular velocity curve, if a regularization parameter $\alpha = 0.02$ is applied. For the dynamical models tested here, the optimal choice of α turns out to be roughly independent of the gravitational potential of the galaxy. The same accuracy as

[3] Here we use r_{SOS} as shorthand for the radii of orbital equatorial crossings, defining the surface of section. Fig. 1 in Thomas et al. (2004) gives an example of a typical surface of section in the actual context. The equatorial crossings locate orbits in the meridional plane fairly well.

for the mass structure is achieved in the reconstruction of internal velocity moments. On the other hand, halo flattening and galaxy inclination are only weakly constrained by our data.

Regularization biases orbit models towards some given idealized galaxy model, assumed to represent the object under study reasonably well. For early-type galaxies, regularization has been commonly implemented to isotropize the final fit. How much regularization is optimal in the reconstruction of a given galaxy depends on the specific data set (spatial coverage, quality) on the one hand and the degree to which the regularization bias approximates the given galaxy on the other. Isotropizing the DF might, for example, be a good recipe for relaxed early-type galaxies but less favourable for lenticulars with a significant, dynamically cold, component. In that case either the value of α or, preferably, the functional form of S, has to be reconsidered. In any case, and for any regularization technique, the optimal balance between the fit to data and smoothing of the DF can be examined case-by-case from simulations similar to those described here.

Cretton et al. (1999) and Verolme & de Zeeuw (2002) have determined optimal regularization for an implementation of Schwarzschild's method with two-integral components by reconstructing similar DFs as used here. The resulting regularization has proven to yield plausible results in subsequent applications (e.g. Cappellari et al. 2002; Verolme et al. 2002; Copin et al. 2004; Cretton & Emsellem 2004; Krajnović et al. 2005). It is difficult to compare quantitatively the amount of regularization applied in these works with the results of our simulations since the regularization techniques differ. However, in each case the achieved accuracy in the recovery of test model parameters and the derived dynamical structure of real galaxies indicate that the applied amount of regularization is comparable.

9.2 Luminous and dark matter in NGC 4807

We applied our code with the simulation-derived regularization to the elliptical NGC 4807. The dynamical models require substantial dark matter in the outer parts of the galaxy. Evidence for dark matter in the form of flat circular velocity curves from (integrated) stellar kinematics of ellipticals has also been found by Rix et al. (1997), Gerhard et al. (1998), Emsellem et al. (1999), Cretton et al. (2000), Kronawitter et al. (2000), Saglia et al. (2000) and Gerhard et al. (2001). Dynamical models of five galaxies with planetary nebulae kinematics complementing stellar kinematics out to $\approx 5\, r_{\rm eff}$ lead the authors to different appraisals: Romanowsky et al. (2003) argue for non-dark matter models consistent with three galaxies observed by the planetary nebulae spectrograph, while Peng, Ford & Freeman (2004) require dark matter in NGC 5128 and the models of NGC 1399 also point at a dark halo (Saglia et al. 2000).

Spherical models for the 21 round ellipticals in the sample of Kronawitter et al. (2000) reveal dark matter fractions of 10–40 per cent at $1\, r_{\rm eff}$ and dark mass equals luminous mass at roughly 2–4 $r_{\rm eff}$ (Gerhard et al. 2001), both comparable to our results for NGC 4807. The halo core density ρ_c of our best-fitting model is about 30 per cent below the predictions of their ρ_c–L_B relation (taking $M_B = -20.76$), although still consistent with it. Among the allowed LOG haloes, however, the core densities vary by a factor of 10 and taking into account NFW fits, even haloes 90 times denser then the best-fitting model are consistent with the data (cf. Fig. 15). From the concentration of our best-fitting (spherical) NFW halo nevertheless a relatively low formation redshift $z_f \approx 2.5$ follows. Still, we need a larger number of flattened ellipticals modelled in sufficient generality to recover the detailed properties and physical origin of their mass distributions.

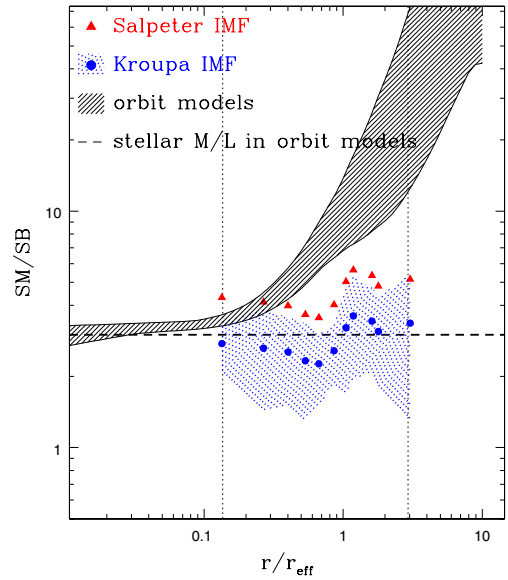

Figure 22. Projected mass-to-light ratio along the major axis of NGC 4807. Hatched area: 68 per cent confidence region of surface mass (SM) over surface brightness (SB) for all orbit models with $\Upsilon = 3.0$ (dashed line). For comparison the projected stellar mass-to-light ratios from population analysis (see text) are shown for two different IMFs: Salpeter IMF (triangles), Kroupa IMF (dots). The dotted area encompasses the statistically allowed Υ based on the Kroupa IMF. For the sake of clarity, the similar, but shifted, error region for the Salpeter-based Υ is omitted.

To cross-check our mass decomposition for NGC 4807 we compared stellar mass-to-light ratios of the orbit superpositions with stellar mass-to-light ratios determined completely independently. In Fig. 22 mass-to-light ratios from stellar population models (Maraston 1998; Thomas, Maraston & Bender 2003; Maraston 2004) of the major-axis spectrum of NGC 4807 (Mehlert et al. 2000, 2003) are compared to the best-fitting orbit models (dashed line: stellar mass-to-light ratio in orbit models; hatched region: 68 per cent confidence region of surface mass SM over surface brightness SB in orbit models; different symbols refer to different initial mass functions (IMFs) underlying the populations). Systematic uncertainties stemming from the unknown IMF are roughly comparable to the statistical errors, indicated for the Kroupa IMF by the dotted area. Only libraries with $\Upsilon = 3.0$ are taken into account in the figure.

As the figure demonstrates, the stellar mass-to-light ratios determined dynamically agree with stellar populations following a Kroupa IMF to $\Delta\Upsilon \approx 0.5$. This (1) confirms our mass decomposition and (2) justifies a posteriori the assumption of a constant stellar mass-to-light ratio. The total surface mass of the dynamical models, as indicated by the shaded region in Fig. 22, exceeds the stellar contribution by far and underlines the evidence for dark matter in NGC 4807. Since our best-fitting orbit models have LOG haloes (or NFW haloes imitating the mass distribution of LOG haloes over the kinematically sampled spatial region) they have maximum stellar mass (e.g. Gerhard et al. 1998). This is in accordance with most previous studies that did not require steep central dark matter profiles (Gerhard et al. 1998; Emsellem et al. 1999; Cretton et al. 2000; Kronawitter et al. 2000; Saglia et al. 2000; Gerhard et al. 2001). On the other hand, Rix et al. (1997) found such profiles consistent with NGC 2434.

9.3 Comparing the kinematics: $\chi^2_{\rm GH}$ versus $\chi^2_{\rm LOSVD}$

The confidence intervals for the structural properties of NGC 4807 have been derived from $\chi^2_{\rm GH}$ as defined in equation (10). However, our models do not explicitly minimize $\chi^2_{\rm GH}$ but instead $\chi^2_{\rm LOSVD}$ as given by equation (8). In order to investigate how the properties of the best-fitting orbit model and the corresponding confidence limits of the halo parameters depend on the choice of χ^2 we have analysed the Monte Carlo simulations as well as the models for NGC 4807 also in terms of

$$\hat{\chi}^2_{\rm LOSVD} \equiv \chi^2_{\rm LOSVD}/\hat{N}_{\rm data}, \tag{11}$$

where $\hat{N}_{\rm data}$ is the number of velocity bins for which $\mathcal{L}^{jk}_{\rm dat} > 0$ (cf. equation 8).

Fig. 23 shows the best-fitting halo parameters and corresponding confidence intervals for the simulated isotropic rotator model of Section 5.3. The figure is as Fig. 10, except that all confidence regions and model-with-data comparisons are computed in terms of $\hat{\chi}^2_{\rm LOSVD}$. Comparing Figs 10 and 23, it turns out that both χ^2-definitions yield identical best-fitting models (designated by the rings in the upper panels, and given by the minima of the two curves in the lower panels). Concerning the confidence regions, however, the computations based on $\hat{\chi}^2_{\rm LOSVD}$ lead to smaller confidence limits for both the logarithmic and the NFW haloes.

For NGC 4807, the analysis based on $\hat{\chi}^2_{\rm LOSVD}$ leads to the results shown in Fig. 24. Again, apart from the different definitions of χ^2, it is as Fig. 14. The best-fitting NFW haloes in Fig. 24 are the same as in Fig. 14. The shapes of the $\hat{\chi}^2_{\rm LOSVD}$ curves for $q = 1.0$ and $q = 0.7$ in the bottom panel of Fig. 24 prefer haloes slightly more concentrated than in the $\chi^2_{\rm GH}$-case, but, as for the isotropic rotator simulations, the differences in the results obtained from $\chi^2_{\rm GH}$ and $\hat{\chi}^2_{\rm LOSVD}$ are small.

Regarding the best-fitting logarithmic halo models (marked by the rings in the upper panels) both χ^2-calculations give consistent, but, in contrast to the Monte Carlo simulations, not identical results. As already indicated in the NFW fits, the logarithmic halo that best fits in the sense of $\hat{\chi}^2_{\rm LOSVD}$ is more concentrated: the dark matter fraction inside $r_{\rm eff}$ is $M_{\rm DM}/M = 0.35$, compared with $M_{\rm DM}/M = 0.22$ for the best-fitting model in the upper panel of Fig. 14. A more striking difference between the upper panels of Figs 14 and 24 is the closure of the 68 per cent $\hat{\chi}^2_{\rm LOSVD}$-confidence contour to the upper right. The contour differences may be related to the ignorance of γ_0 in equation (10), since the mismatch between model and data intensities progressively increases from the lower left to the upper right in the upper panel of Fig. 14.

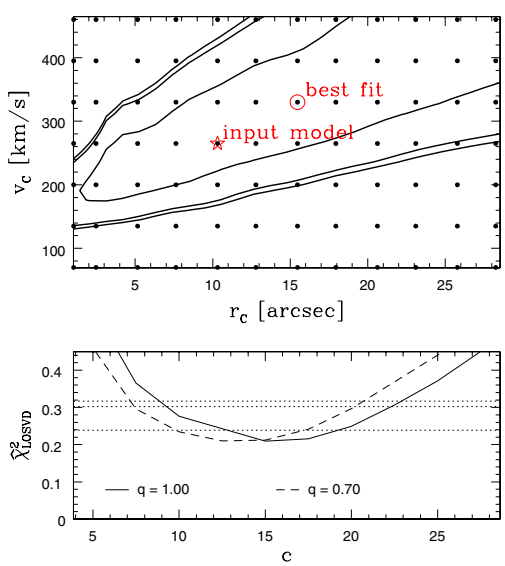

Figure 23. As Fig. 10, but the confidence regions are derived from $\hat{\chi}^2_{\rm LOSVD}$ (see Section 3.5).

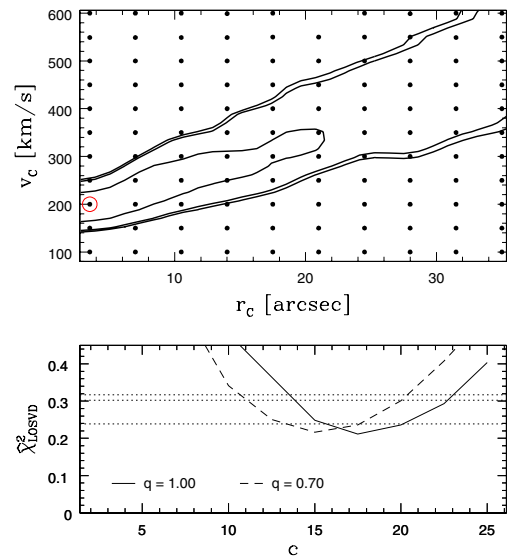

Figure 24. As Fig. 14, but the confidence regions are derived from $\hat{\chi}^2_{\rm LOSVD}$ (see Section 3.5).

Nevertheless, the comparison of the results obtained from $\chi^2_{\rm GH}$ and $\hat{\chi}^2_{\rm LOSVD}$ reveals that both methods – within the errors – give the same results. The confidence limits quoted in this paper, based on equation (10), are the more conservative choice, but may be slightly too pessimistic.

9.4 The outer parts of NGC 4807

Based on a recent refinement (Thomas et al. 2004) of the Schwarzschild code of Richstone & Tremaine (1988) and Gebhardt et al. (2000), we recovered a depopulation of retrograde, near-circular orbits in the phase-space DF of NGC 4807, giving rise to a keel when plotting orbital phase-space densities against orbital energy. The prograde counterparts of the depopulated orbits form a dumbbell-like structure extending about $\approx 2\, r_{\rm eff}$ above the equatorial plane.

To investigate what might cause the depopulation of retrograde orbits in the outer parts of NGC 4807, we projected a sequence of distribution functions in which all orbits involved in the keel ($w_i^+/w_i^- > 99$, see Section 8) are repopulated according to

$$\begin{aligned} w^+_{i,\rm new} &\equiv \xi \times \left(w_i^+ + w_i^-\right) \\ w^-_{i,\rm new} &\equiv (1-\xi) \times \left(w_i^+ + w_i^-\right). \end{aligned} \tag{12}$$

Since $w^+_{i,\rm new} + w^-_{i,\rm new} = w_i^+ + w_i^-$ this does not alter the fit to the luminosity profile but just levels the relative fraction ξ of light on the prograde and retrograde specimen of all keel-involved orbit pairs. Roughly speaking, equation (12) transforms the keel into a narrow cloud of points parallel to the mainstream DF with an offset increasing with $|\xi - 0.5|$. Fig. 25 shows the resulting projected (major-axis) kinematics for $\xi = 0.7$, 0.94, 1.0. As expected, shifting light from prograde to retrograde orbits reduces the amount of rotation v and lowers H_3 in the outer parts, while at the same time leading to a larger velocity dispersion σ and enhanced H_4. As shown by the

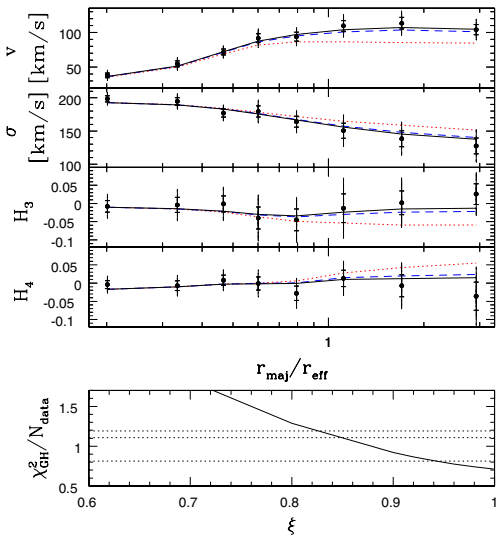

Figure 25. Upper panel: projected major-axis kinematics of three distribution functions calculated in the gravitational potential of the best-fitting mass model: (1) all retrograde orbits in the keel depopulated completely (solid); relative fraction of light on prograde keel-orbit counterparts (2) $\xi = 0.94$ (short-dashed) and (3) $\xi = 0.7$ (dotted). Lower panel: goodness of fit (including the minor-axis LOSVDs, which are not affected by the redistribution of keel-involved orbits) as a function of the relative fraction ξ of light on prograde keel-orbit correspondents; horizontal dotted lines indicate 68, 90 and 95 per cent confidence levels.

goodness of fit in the lower panel of Fig. 25, the best fit to the data is achieved for $\xi = 1.0$ (all retrograde keel orbits completely depopulated). Comparing the corresponding solid lines in Fig. 25 with the upper panel of Fig. 12 reveals that $\xi = 1.0$ provides essentially the same fit as the best-fitting orbit model. Consequently, the retrograde keel orbits can be regarded as completely depopulated in our models of NGC 4807. Reducing the relative fraction of light on the prograde counterparts of keel orbits to $\xi = 0.94$ is only consistent with the observations at the 68 per cent confidence level. A further equalization to $\xi = 0.7$ is already incompatible with the observed velocity profiles.

The outer major-axis LOSVDs of NGC 4807 might indicate weak triaxiality, for example in the form of a weak, nearly end-on bar (e.g. Bureau & Athanassoula 2005). A weak bar-like structure would also fit the boxy appearance of the outer isophotes of the galaxy. Assuming that NGC 4807 is slightly triaxial, the keel in the DF might be an artefact of the assumption of axisymmetry. Note, however, that NGC 4807 is consistent with being axisymmetric, albeit then the depopulation of single orbit families, especially around the equatorial plane, is hard to understand in the course of dynamical processes.

Depopulation of retrograde orbits in the outer parts of the galaxy is accompanied by a change in stellar ages from $\tau \approx 5$ Gyr inside $r < r_{\rm eff}$ to $\tau \approx 10$ Gyr at larger radii (Mehlert et al. 2003). Towards $3\,r_{\rm eff}$ stellar ages become uncertain and no clear trend is visible. It also seems possible that the keel in the DF is an artefact related to a distinct stellar component and an associated (slight) change in Υ. It should be noted that because the orbit models are fitted to deprojections and stellar kinematics, the derived DFs characterize the amount of *light* per volume element in phase space, not the *mass* density in phase space. Accordingly, depressions in the DF might (at least partly) reflect enhanced Υ.

A distinct stellar component in the outer parts must not necessarily take the form of a bar, but could also be a faint axisymmetric stellar disc. Indeed, the photometry as well as the orbit models suggest that NGC 4807 is close to edge-on, but a dynamically cold, outer stellar disc made of only 0.7 per cent prograde orbits at latitudes $\vartheta < 10^\circ$ (see Section 8) is consistent with the non-discy isophotes ($\max a_4 < 1$). A disc carrying 2 per cent of the total luminosity would show up with $\max a_4 \approx 4$ when seen exactly edge-on and $\max a_4 < 1$ for such a disc would require $i < 75^\circ$ (Rix & White 1990). From our simulations it seems impossible to distinguish kinematically between $i = 70^\circ$ and $i = 90^\circ$ and, consequently, there is some freedom for an outer disc in NGC 4807.

In any case further investigations are necessary to verify the significance of the keel structure in the DF of NGC 4807. (1) Kinematic measurements along intermediate position angles in the galaxy would likely put more constraints on the DF. (2) Detailed comparison of orbit superpositions with realistic galaxy models are required to estimate how relics of triaxiality, faint discs and multicomponent (multi-Υ) structures show up in our axisymmetric models. These questions will be addressed in a forthcoming publication.

9.5 Internal stellar kinematics of NGC 4807

Along the major axis, NGC 4807 is mildly radially anisotropic. Radial anisotropy has been found in a number of ellipticals (Gerhard et al. 1998; Matthias & Gerhard 1999; Cretton et al. 2000; Gebhardt et al. 2000; Saglia et al. 2000). The amount of anisotropy ($\beta \approx 0.3$) in the outer parts as well as the isotropy of the central region (inside $0.3\,r_{\rm eff}$) matches the typical anisotropy structure found for round, non-rotating ellipticals by Gerhard et al. (2001). Along the minor axis, NGC 4807 is dominated by tangential motions. Gebhardt et al. (2003) report tangential anisotropy for some galaxies (mostly enhanced azimuthal, but suppressed meridional dispersions) and also Dejonghe et al. (1996), Cretton & van den Bosch (1998), Statler et al. (1999), Cappellari et al. (2002), Verolme et al. (2002) and Copin et al. (2004) find predominantly tangential motions. For NGC 3115, Emsellem et al. (1999) notice $\sigma_z > \sigma_r$. All these studies are based on data sets with different spatial sampling and use various dynamical modelling techniques, particularly differing in the amount and functional form of the applied regularization. As for the mass structure and the dark matter properties, a large and homogeneous sample of galaxies is needed to address the physical processes shaping elliptical galaxies.

ACKNOWLEDGMENTS

We thank the referee, Tim de Zeeuw, for constructive comments that helped to improve the manuscript. JT acknowledges financial support by the Sonderforschungsbereich 375 'Astro-Teilchenphysik' of the Deutsche Forschungsgemeinschaft.

REFERENCES

Bender R., Möllenhoff C., 1987, A&A 177, 71
Binney J., Tremaine S., 1987, Galactic Dynamics. Princeton Univ. Press Princeton
Bureau M., Athanassoula E., 2005, ApJ, in press (astro-ph/0403226)
Cappellari M., Verolme E. K., van der Marel R. P., Verdoes Kleijn G. A., Illingworth G. D., Franx M., Carollo C. M., de Zeeuw P. T., 2002, ApJ, 578, 787
Carollo C. M., de Zeeuw P. T., van der Marel R. P., Danziger I. J., Qian E. E., 1995, ApJ, 441, L25
Colin P., Avila-Reese V., Valenzuela O., 2000, ApJ, 542, 622
Copin Y., Cretton N., Emsellem E., 2004, A&A, 415, 889
Cretton N., van den Bosch F. C., 1998, ApJ, 514, 704

Cretton N., Emsellem E., 2004, MNRAS, 347, L31
Cretton N., de Zeeuw P. T., van der Marel R. P., Rix H. W., 1999, ApJS, 124, 383
Cretton N., Rix H. W., de Zeeuw P. T., 2000, ApJ, 536, 319
Davé R., Spergel D. N., Steinhardt P. J., Wandelt B. D., 2001, ApJ, 547, 574
de Blok W. J. G., McGaugh S. S., Bosma A., Rubin V. C., 2001, ApJ, 552, L23
Dehnen W., Gerhard O. E., 1994, MNRAS 268, 1019
Dejonghe H., de Bryne V., Vauterin P., Zeilinger W. W., 1996, A&A, 306, 363
Emsellem E., Dejonghe H., Bacon R., 1999, MNRAS, 303, 495
Gebhardt K. et al., 2000, AJ, 119, 1157
Gebhardt K. et al., 2003, ApJ, 583, 92
Gentile G., Salucci P., Klein U., Vergani D., Kalberla P., 2004, MNRAS, 351, 903
Gerhard O. E., 1993, MNRAS, 265, 213
Gerhard O. E., Binney J., 1996, MNRAS, 279, 993
Gerhard O. E., Jeske G., Saglia R. P., Bender R., 1998, MNRAS, 295, 197
Gerhard O. E., Kronawitter A., Saglia R. P., Bender R., 2001, AJ, 121, 1936
Häfner R., Evans N. W., Dehnen W., Binney J., 2000, MNRAS, 314, 433
Jing Y. P., Suto Y., 2000, ApJ, 529, L69
Knebe A., Devriendt J. E. G., Mahmood A., Silk J., 2002, MNRAS, 329, 813
Kormendy J., Bender R., 1996, ApJ, 464, 119
Krajnović D., Cappellari M., Emsellem E., McDermid R. M., de Zeeuw P. T., 2005, MNRAS, 357, 1113
Kronawitter A., Saglia R. P., Gerhard O. E., Bender R., 2000, A&AS, 144, 53
Lynden-Bell D., 1967, MNRAS, 136, 101
Magorrian J., Binney J., 1994, MNRAS, 271, 949
Magorrian J., 1999, MNRAS, 302, 530
Maraston C., 1998, MNRAS, 300, 872
Maraston C., 2004, preprint (astro-ph/0410207)
Matthias M., Gerhard O. E., 1999, MNRAS, 310, 879
Mehlert D., Saglia R. P., Bender R., Wegner G., 2000, A&AS, 141, 449
Mehlert D., Thomas D., Saglia R. P., Bender R., Wegner G., 2003, A&A, 407, 423
Merritt D. R., 1993, ApJ, 413, 79
Moore B., Quinn T., Governato F., Stadel J., Lake G., 1999, MNRAS, 310, 1147
Navarro J. F., Frenk C. S., White S. D. M., 1996, ApJ, 462, 563
Navarro J. F. et al., 2004, MNRAS, 349, 1039
Peng E. W., Ford H. C., Freeman K. C., 2004, ApJ, 602, 685
Qian E. E., de Zeeuw P. T., van der Marel R. P., Hunter C., 1995, MNRAS, 274, 602
Richstone D. O., Tremaine S., 1988, ApJ, 327, 82
Rix H. W., White S. D. M., 1990, ApJ, 362, 52
Rix H. W., de Zeeuw P. T., Cretton N., van der Marel R. P., Carollo C. M., 1997, ApJ, 488, 702
Romanowsky A. J., Douglas N. G., Arnaboldi M., Kuijken K., Merrifield M. R., Napolitano N. R., Capaccioli M., Freeman K. C., 2003, Sci, 301, 1696
Rybicki G., 1987, in de Zeeuw T., ed., Proc. IAU Symp. 127, Structure and Dynamics of Elliptical Galaxies. Reidel, Dordrecht, p. 397
Saglia R. P., Kronawitter A., Gerhard O. E., Bender R., 2000, AJ, 119, 153
Schwarzschild M., 1979, ApJ, 232, 236
Statler T. S., Dejonghe H., Smecker-Hane T., 1999, AJ, 117, 126
Swaters R. A., Madore B. F., van den Bosch F. C., Balcells M., 2003, ApJ, 583, 732
Thomas D., Maraston C., Bender R., 2003, MNRAS, 339, 897
Thomas J., Saglia R. P., Bender R., Thomas D., Gebhardt K., Magorrian J., Richstone D., 2004, MNRAS, 353, 391
Valluri M., Merritt D., Emsellem E., 2004, ApJ, 602, 66
van der Marel R. P., Franx M., 1993, ApJ, 407, 525
Verolme E. K., de Zeeuw P. T., 2002, MNRAS, 331, 959
Verolme E. K. et al., 2002, MNRAS, 335, 517
Wechsler R. H., Bullock J. S., Primack J. R., Kravtsov A. V., Dekel A., 2002, ApJ, 568, 52
Wegner G., Corsini E. M., Saglia R. P., Bender R., Merkl D., Thomas D., Thomas J., Mehlert D., 2002, A&A, 395, 753
Zhao H. S., 1996, MNRAS, 283, 149

This paper has been typeset from a TEX/LATEX file prepared by the author.